Three-dimensional disordered alloy metamaterials: a new platform of structure-function integration

OPEN ACCESS
IOP Publishing | Songshan Lake Materials Laboratory

MATERIALS FUTURES

Mater. Futures 4 (2025) 012001 (21pp)

https://doi.org/10.1088/2752-5724/ada172

Topical Review

Three-dimensional disordered alloy metamaterials: a new platform of structure-function integration

Xinxin Li[1,3], **Liqiang Wang**[2,3] **and Yang Lu**[1,*]

[1] Department of Mechanical Engineering, The University of Hong Kong, Hong Kong Special Administrative Region of China, People's Republic of China
[2] Department of Mechanical Engineering, City University of Hong Kong, Hong Kong Special Administrative Region of China, People's Republic of China

E-mail: ylu1@hku.hk

Received 16 October 2024, revised 22 November 2024
Accepted for publication 12 December 2024
Published 13 January 2025

Abstract

Metamaterials have garnered significant interest in recent years due to their unprecedented properties unattainable by natural substances and potential applications in various fields. In this review, we provide an in-depth analysis of a novel class of three-dimensional (3D) disordered alloy metamaterials, including metallic glasses and high/medium entropy alloys metamaterials, which offer a promising platform for the integration of structure and function. These materials are characterized by their unique including disordered atomic structures and alloy compositions modulation, enabling the manipulation of electromagnetic, thermal, and mechanical properties. We begin by discussing the underlying principles and synthesis methods of 3D disordered alloy metamaterials, followed by a comprehensive examination of their distinctive properties and potential applications in the realms of engineering, energy harvesting, and sensing. Furthermore, we delve into the existing challenges and future directions of this burgeoning field, encompassing aspects such as scalability, precision in fabrication, and the evolution of multi-functional materials. 3D disordered alloy metamaterials represent a promising avenue for the advancement of structure-function integration, with potential implications for a broad range of scientific and technological disciplines.

Keywords: metamaterials, metallic glasses, high/medium entropy alloys, micro/nanolattices, fabrication techniques, mechanical properties, multifunctional performance

[3] These authors contributed equally to this work.
[*] Author to whom any correspondence should be addressed.

1. Introduction

1.1. Background of disordered alloy

Novel types of disordered metallic materials, such as metallic glasses (MGs) and high entropy alloys (HEAs), have garnered significant interest in recent decades [1–8]. This attention is attributed to two primary factors: (i) their inherently disordered local structures and chemistries offer a diverse and intricate landscape, making them ideal candidates for examining the fundamental structure-property relationship in materials science; (ii) their metastable properties present immense potential for performance manipulation, paving the way for a plethora of engineering applications. Specifically, the four core effects of HEAs have been elucidated [7, 9]. These effects can lead to alterations in electronic conditions [10], reductions in energy formation within specific states [11], distortions that induce changes in lattice parameters [12], enhanced ionic diffusivity [13], and modifications in mechanical properties [14]. MGs endow them with distinct characteristics [15], including: (i) isotropy, with catalytic active centers uniformly dispersed in a singular form within the chemical environment [16, 17]; (ii) a liquid-like region on the surface, characterized by elevated surface energy, a high concentration of complex, unsaturated sites, formidable activation capacity, and a dense distribution of active centers [3, 18, 19]; (iii) a broad modulation range for components and electronic structures, facilitating the acquisition of suitable catalytic active centers [20–22]; (iv) an absence of traditional crystal alloy defects, resulting in high strength and elasticity [23–25].

Both disordered alloys exhibit remarkable structural properties, such as elevated yield strength and fracture toughness, as demonstrated in figure 1. In a significant development within materials science, Miao *et al* [19, 26, 27] recently achieved this using atomic resolution electron tomography. This method entails passing an electron beam through a sample to obtain a 2D projection of its three-dimensional (3D) atomic structure. By altering the sample's orientation relative to the electron beam, a series of 2D images is generated, which are subsequently reconstructed into a comprehensive 3D image of the sample. This experiment has confirmed the presence of structural and chemical disorder in MGs and HEAs, thus providing novel insights into understanding disordered solid structures and the development of new alloy compositions.

1.2. The significance of structure-function integration

High-performance components are predominantly employed in harsh environments and typically exhibit characteristics such as exceptional load-bearing capacity, extreme heat resistance, ultra-precision, ultra-lightweight, and high reliability [29]. These components serve as core elements in major equipment, including hypersonic vehicles, launch vehicles, orbital space stations, and nuclear fusion devices. Presently, the design and manufacturing of high-performance components face three main challenges due to the coupled influences of material, structure, and process: first, the complex coupling effect of material distribution and multi-scale structural characteristics on component performance complicates the design of matching component materials and structures. Second, traditional design methods and manufacturing processes constrain the comprehensive manufacturing of complex components. Third, the absence of precise forming control methods necessitates repeated trial and error, leading to difficulties in controlling high-performance targets.

Integrated material-structure design and manufacturing presents an effective solution to these challenges [30]. Advanced structures are evolving towards multi-functional integration, wherein multi-functional structures can provide various functions such as damping, vibration reduction, stealth, and conduction, in addition to fulfilling basic load-bearing requirements [7, 15]. Rational structure configuration design and multi-function realization can effectively enhance structural performance. By employing additive/subtractive/equal materials composite manufacturing, it is possible to create new structures with complex configurations and multi-material composites, thereby achieving components that possess both load-bearing and additional functional capabilities. The design and manufacturing of functional structures hold significant research value and have attracted widespread attention. For instance, thermal structure technology is fundamental to high-speed aircraft. As flight speeds and durations increase, high-speed aircraft are subject to increasingly stringent mechanical and thermal environments. Consequently, enhancing aircraft performance necessitates the swift realization of lightweight and efficient structures [29]. Traditional aircraft structures, designed for load-bearing and heat-protection functions, primarily employ ablation, heat sink, insulation, and radiation for heat-protection. These structures, however, are single-function and struggle to meet the evolving demands of high-speed aircraft. The new generation of thermal protection structures is transitioning from single to multi-functional, integrated structures that work in unison and manage energy. These structures not only need to demonstrate high-temperature resistance, high strength, and robust environmental stability, but also incorporate load-bearing capacity, wave penetration, heat protection, and energy management functions. The integrated thermal protection/load-bearing structures take various forms, such as corrugated sandwich and lattice structures. Concurrently, structures based on bionics, such as honeycomb structures, lotus-root inspired structures, and horn-leaf bionic folds, are also being developed.

1.3. Advantages of metamaterials in structure-function integration

The promotion of civilization is intrinsically linked to the development of human tools, which in turn, is substantially influenced by the usage of newfound materials, like wood,

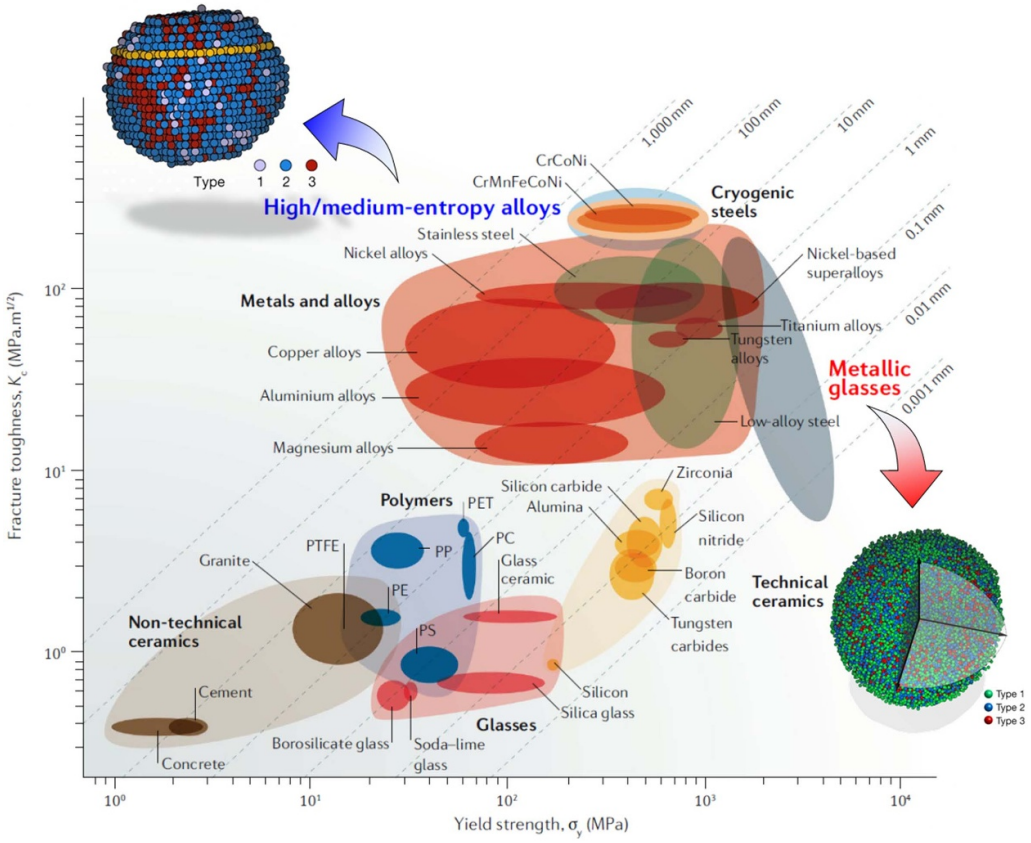

Figure 1. Ashby plot of yield strength versus fracture toughness showing that high/medium entropy alloys and metallic glasses are most superior mechanical properties materials on record. Reproduced from [28], with permission from Springer Nature. The insets experimentally indicate that disorder exists in high entropy alloys (top-left panel, chemical disorder) and metallic glasses (bottom-right panel, structural disorder). Reproduced from [27], with permission from Springer Nature. Reproduced from [26], with permission from Springer Nature. The atomic numbers of certain species were so close that they could not be differentiated. The constituent elements are grouped into three categories: type 1 includes cobalt and nickel (atomic numbers 27 and 28); type 2 comprises ruthenium, rhodium, palladium, and silver (atomic numbers 44–47); and type 3 consists of iridium and platinum (atomic numbers 77 and 78).

metals, and textiles. The attributes of these materials significantly determine the functionality of the tools, leading scientists to aspire to create synthetic materials with controllable attributes. In response, mechanical metamaterials have been proposed. These are engineered materials with deliberately designed microstructural components, providing exceptional mechanical properties.

During the past two decades, the advent of mechanical metamaterials has opened up a new avenue for exploring the advanced functionalities that can be integrated into mechanical materials and structures. Extending the scope of mechanical metamaterials beyond machinery to achieve multifunctionality is a challenging and active area of research within the field [31]. The next generation of mechanical metamaterials is moving towards integrated systems, and it is anticipated that further research will optimize their functions and expand their application domains. Materials science is increasingly steering the direction of structural materials, particularly with the use of functional materials to obtain mechanical metamaterials with active, adaptive, and actuating capabilities. For instance, electromechanical, thermomechanical, magneto–mechanical, or opto–mechanical materials are utilized in mechanical metamaterials with the objective of achieving tunable, adaptive responses that are driven by external stimuli. Within this context, HEAs and MGs play a crucial role.

2. Brief overview of different types of metamaterials

The concept of metamaterials originated in the electromagnetic field, with artificially designed materials used to modulate the polarization of radio waves, known as electromagnetic metamaterials [32]. This concept was subsequently extended to other fields such as acoustic, optical, and thermal metamaterials [33]. In recent years, typical metamaterials such as left-handed materials [34, 35], 'invisibility cloaks' [36, 37], and perfect lenses [38–40] have emerged in optics, communications, defense, and other applications. A host of electromagnetic, mechanical, acoustic, thermal metamaterials and novel

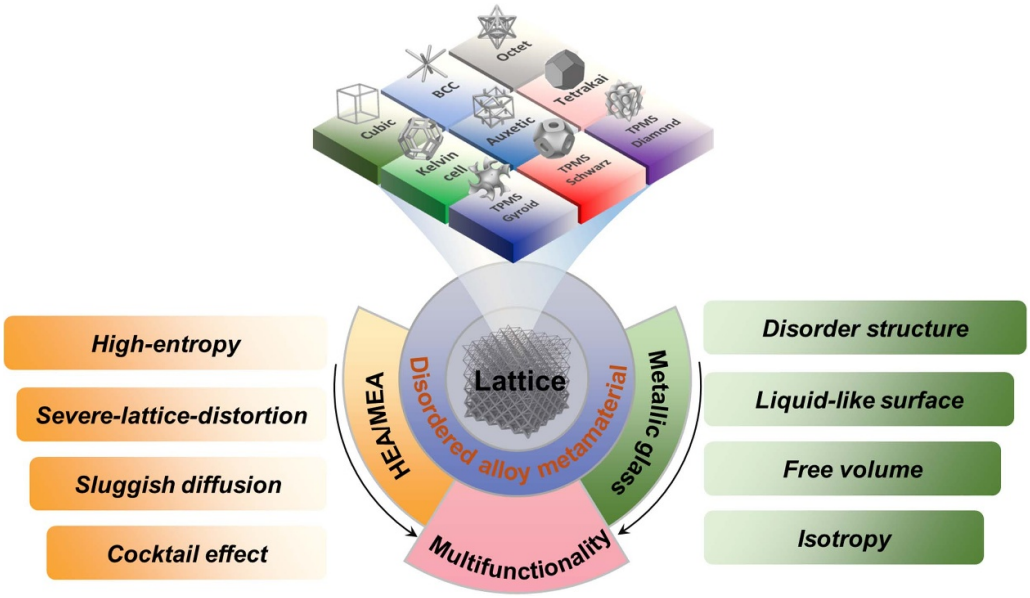

Figure 2. Illustration of disordered alloy metamaterials as a platform of structure-function integration.

materials based on the fusion of metamaterials and traditional materials have emerged, forming a significant growth point for new materials.

According to the different basic geometric forms of structures, metamaterials of different applications can be mainly divided into beam, plate and shell metamaterials, corresponding to the geometric forms of lines, planes, and surfaces, respectively (figure 2). Each type of lattice metamaterial has unique characteristics. For instance, shell metamaterials composed of curved surfaces typically have higher specific stiffness and specific energy absorption under low-density conditions than beam and plate lattice materials. However, despite their excellent mechanical properties, shell lattice materials typically exhibit less variation in their topological structures, and adjustability is usually limited to shell thickness and structural shape. Furthermore, design space and freedom are limited when optimizing the design of shell lattice materials, whether through topology optimization, shape optimization, or size optimization. As a result, the performance improvement of the optimization results is also limited [41]. This review primarily focuses on the manifestation and influence of the combination of two types of disordered alloys and metamaterials in the application of structure-function integration (figure 2), and thus does not give much attention to topological optimization of structures, despite it being an important branch of metamaterial research.

3. Fabrication techniques

Metamaterials are a unique category of synthetic materials that possess extraordinary physical properties, primarily derived from meticulously engineered microscopic structures. These physical properties can manifest as a negative refractive index, perfect lenses and even invisibility. Research and practical applications of metamaterials are significantly influenced by the fabrication techniques used, as these directly affect the microstructure and properties of the metamaterials. Precision material processing is a prerequisite for the fabrication of metamaterials, and the development of certain electromagnetic metamaterials, especially those operating at frequencies above the terahertz range, depending on the advancement of associated processing technologies.

Achieving the desired physical properties requires precise control over the material's structure at the micro or nanometer scale. A variety of advanced fabrication techniques are currently available to produce metamaterial, allowing precise manipulation of the material's structure at an extremely small scale, facilitating the creation of the desired physical properties. In particular, 3D printing technology has emerged as an important method for metamaterial fabrication due to its ability to create intricate microstructures. However, the fabrication technology also influences the cost and scalability of metamaterial production. Some techniques may require expensive equipment or time-consuming processes, limiting the commercial viability of metamaterials. As a result, the scientific community is actively seeking more cost-effective and efficient production methods. This study focuses primarily on alloy metamaterials, and figure 3 provides a comparative analysis of the resolution of different alloy metamaterial fabrication techniques at commercial and laboratory scales. There is currently no standard classification of metamaterial fabrication techniques. This review categorizes the methods based on the metamaterial manufacturing pathway, including mainly direct printing, electroassisted deposition, template and photolithography.

Direct printing methods involve the build-up of material layer by layer to create objects with complex microstructures. Norsk Titanium [42] has developed a method for the rapid production of bulk metal products by rapidly heating wires with

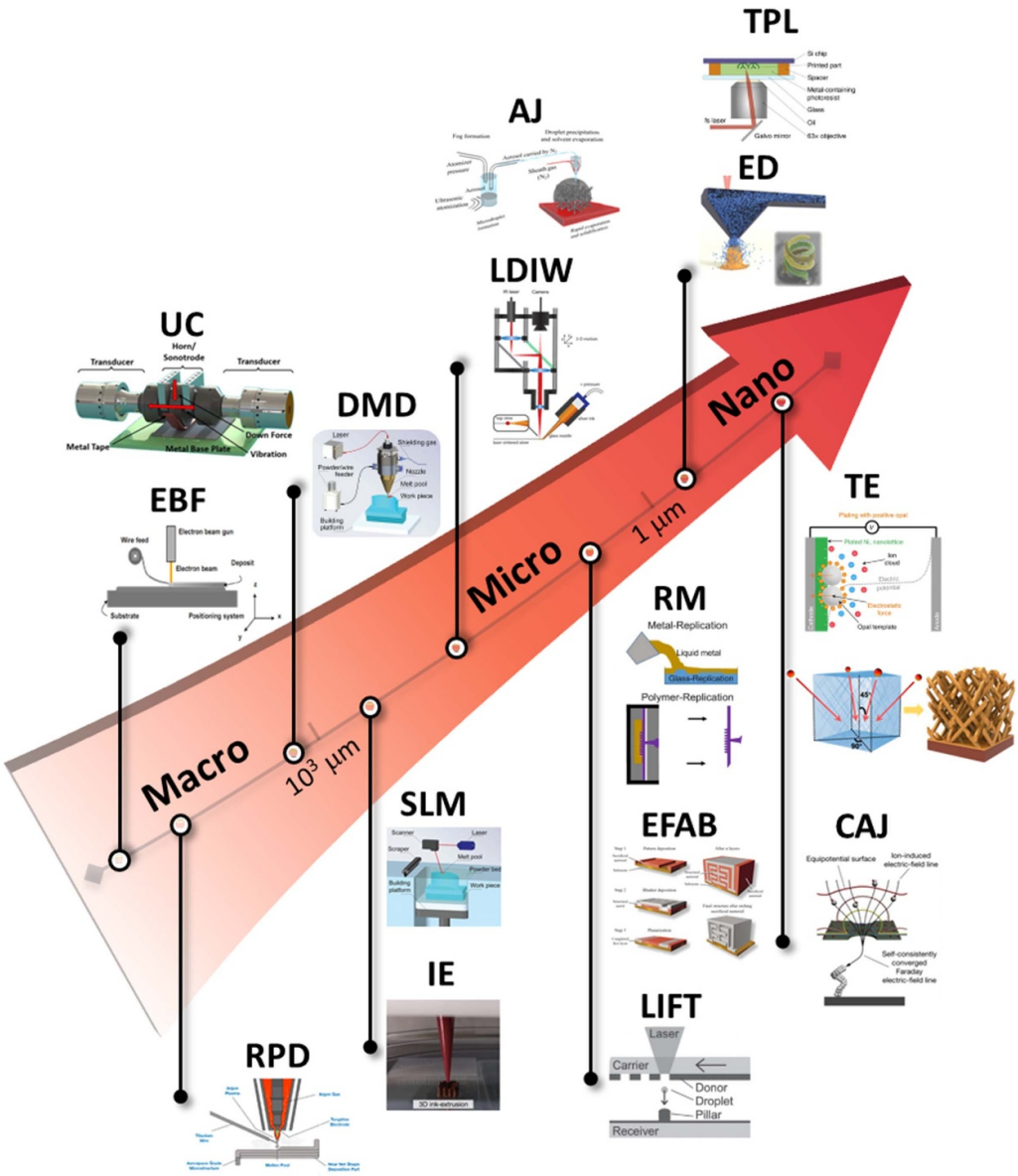

Figure 3. Diversity of minimum feature sizes for commercial and potentially metal manufacturing technologies. Table 1 is referred to the detailed data. UC, EBF, RPD, and DMD are ultrasonic consolidation, electron beam free form fabrication, rapid plasma deposition, and direct metal deposition respectively. SLM, IE, AJ, LDIW, RM, EFAB, and LIFT are selective laser melting, ink extrusion, aerosol jet, laser-assisted direct ink writing, replicative manufacturing, electrochemical fabrication, and laser-induced forward transfer respectively. TPL, ED, TE, and CAJ are two-photon lithography, electrochemical deposition, template electroplating, and charged aerosol jet respectively.

plasma in an argon atmosphere, forming layers 3–4 mm high and 8–12 mm wide. Compared to powder-based 3D printing, RPD produces rougher surfaces but works much faster, almost 50–100 times faster. Monitoring the production process 600 times per second results in a high standard of consistency. Ultrasonic metal welding is based on oxide fracture under pressure, which allows new metal surfaces to bond and shear-induced non-uniform plastic deformation of the surface to promote dynamic recrystallization of the interface microstructure, forming a narrow welding area with a size of about 10–20 μm. And the overall temperature is much lower than the melting temperature of metal [43, 44].

Laser cladding is a prevalent metal additive manufacturing (AM) method due to its domain-by-domain local forming characteristics, enabling the printing process and performance control requirements to span over six orders of size magnitude. Currently, the two primary representative categories are laser Directed Energy Deposition (DED) and laser powder bed fusion [45]. The thickness of the deposited layers in DED is typically no more than 1 mm and can be as small as several hundred microns [46]. One distinguishing feature of DED is its rapid manufacturing capability, allowing for the construction of large components. Another characteristic is its high degree of flexibility, extending its applicability to surface

Table 1. Resolutions of various of manufacturing technologies.

Manufacturing technologies	Layer thickness range (μm)	References
Ultrasonic consolidation	1500	[44]
Electron beam free form fabrication	3000	[42]
Rapid plasma deposition	3000	[42]
Direct metal deposition	1000	[45]
Selective laser melting	100	[45]
Ink extrusion	100	[50, 51]
Aerosol jet	10	[62]
Laser-assisted direct ink writing	10	[53]
Replicative manufacturing	5	[58]
Electrochemical fabrication	4	[60]
Laser-induced forward transfer	4	[63]
Two-photon lithography	0.5	[42]
Electrochemical deposition	0.8	[54]
Template electroplating	0.1	[59]
Charged aerosol jet	0.085	[55, 56]

coating [47], repair [48], and rapid prototyping [48]. However, the accuracy of DED metal parts is low, necessitating subsequent processing to meet the structural and accuracy requirements of the design. Additionally, the delamination process imposes a thermal history, leading to inter-dendrite segregation, microstructure gradients of the elements, and thermal cracks [49].

Ink extrusion is a technique that involves the formation of an element or pre-alloying powder at ambient temperature within a binder-containing green billet. This method can circumvent alloy segregation issues, reduce costs, and eliminate the need for an inert gas processing environment required for beam-based AM. Moreover, full interdiffusion and isothermal sintering in this process result in low residual stress. Dunand *et al* [50, 51] used 3D extrusion of ink comprising a mixture of oxide nanoparticles, which were then co-reduced to metal in hydrogen atmosphere, diffused, and fired to form a near full-density face-centered cubic equiatomic ratio CoCrFeNi alloy. This resulted in a CoCrFeNi microcrystal lattice beam with diameters of 100 μms, demonstrating superior mechanical properties and low-temperature performance in certain environments. Laser-assisted ink direct writing can further reduce the resolution and improve the printing speed of ink direct writing to less than 1 μm s^{-1}. One example of this approach is the meniscus-confined 3D electrodeposition for direct writing of wire bond [52]. By combining the printing of concentrated silver nanoparticle inks with focused infrared laser annealing, Skylar–Scott *et al* has been able to quickly create high conductivity and ductility metal microarrays [53]. This preparation method has three advantages: (i). by integrating the patterning and annealing processes, the printed metal features display the necessary mechanical properties required for accurately manufacturing arbitrary objects in the air, allowing for the creation of complex curved structures without the need for supporting materials; (ii). local annealing enables these features to be printed on inexpensive plastic substrates like polyethylene terephthalate (PET).; (iii). The pattern features high electrical conductivity, comparable to that of bulk silver.

Most of the existing metal AM methods are limited to resolutions of about 20–50 μm, which makes it challenging to generate complex 3D printed metal structures with smaller features. Vyatskikh *et al* [42] has developed a process to create a resolution based on lithography of about 100 nm complex 3D nanostructures metal. In this process, two-photon lithography was used to carve 3D polymer scaffolds, which were pyrolyzed to remove volatile organic matter, resulting in metamaterials with >90 wt% nickel content. Nanomechanical experiments show that its specific strength is 2.1–7.2 MPa g^{-1} cm^3, which is comparable to the lattice structures produced by current metal AM techniques. This study presents an efficient method for 3D printing microstructure and nanostructured metals with sub-micron resolution.

Electroassisted deposition is an emerging microfabrication method that offers potential advantages in manufacturing at the micron scale and below. The approach proposed by Hirt *et al* [54] is based on microchannel Atomic Force Microscope cantilevers with an aperture at the tip. However, unlike other pipette-based methods, there is no need to calibrate the print speed because growth is automatically detected by force feedback. This technique could be particularly beneficial for manufacturing at the micron scale and below, where there may be potential for throughput to be increased through parallelization. Liu *et al* newly developed 'Faraday 3D printing' is a new paradigm for micro and nano processing that combines nanometer accuracy, 3D features, and parallel array processing [55]. This approach involves the use of electric nano brushes and controlled array configurations to realize the coupling field control [56, 57]. Due to the small building blocks (a few of atoms to a few of nanometers) involved, the printed structures exhibit high uniformity and excellent structural performance. Furthermore, any material can be printed if the charge number and size are precisely controlled. Unlike lithography, which is limited by the lower limit of the wavelength size of the light source, the size of the power line brush is not limited, allowing for feature sizes down to the atomic scale range. The ability to

array parallel printing holds promise for breakthroughs in the field of micro and nano AM.

In contrast to most direct forming methods, which are limited by the reaction time of the preparation, tool-based manufacturing processes enable rapid, high-quality mass production. Kluck *et al* has proposed a type of casting by fused silica template and replication technology to manufacture for tool-based with smooth surface of metal insert technology [58]. The replication of bronze, brass, and cobalt–chromium alloys using fused silica molds has been successfully achieved, resulting in a surface roughness of 8 nm and a microstructure size of approximately 5 μm. The injection molding process was conducted using a commercially available system, which enabled the production of thousands of replicas with the identical mold. Jiang and Pikul [59] combined with template method and electroplating can further reduce the resolution of metal microlattice. By keeping the template wet and using electrostatic-assisted metal deposition through the template to eliminate cracks in the self-assembly process, centimeter-scale multifunctional metal nanolattices with a 100 nm period feature and 30 nm grain size are fabricated, representing a 20 000-fold increase in the crack-free area. The number of cells has been increased 1000-fold compared to previous nanolattices, with the cells in the loading direction. Similarly, stencils can be prepared by lithography, which has great advantages in forming micro–nano-fine structures and devices, but the process is time consuming and harsh preparation conditions [60].

In the search for efficient forming technologies, nature also provides us with a great deal of inspiration. Petal-like gypsum crystals found in the deserts of West Africa, known as 'desert roses,' are formed by evaporation of the solvent by desert heat [61]. Saleh *et al* [62] sought to emulate the natural process in a controlled manner, creating 3D microarchitectural structures through the dispersion of silver nanoparticles in an ethylene glycol aqueous solution. It is important to note that despite the ability of aerosol jet printing to achieve more refined droplet sizes and characteristics, this process is not reliant on the method used for droplet generation. The microarchitecture is manifested as a network of interconnected truss elements, oriented at varying angles relative to the horizontal plane. These elements can be as thin as 20 μm in diameter, with the open spaces within the printed structure ranging from 100 μm to 1 μm. Furthermore, the bombardment of the material enables the construction of the metal micro–nano lattice. Visser *et al* [63] employed a pulse laser focus on the 200 nm-thick layer of copper donor, thereby injecting liquid copper drops. By oscillating the glass carrier in a horizontal plane, repeated ejections are induced at the same location. The impact droplets solidify, thus forming columns on the receiving substrate. To enhance the adhesion of the droplets, the receiver is coated with a copper film. Each ejection results in the formation of a hole in the donor membrane, which is referred to as a 'crater.' This crater is deposited in a matter of minutes by moving the receiver and repeating a series of ejection events. The implementation of an automatic positioning phase for the receiver would facilitate the deposition of column forests or complex microstructures. This method is theoretically suitable for all alloy materials, with the high cooling rate being particularly useful for preparing metastable phases [64, 65], including MGs [64].

In a word, preparation technology occupies a pivotal position in the field of metamaterials, being of paramount importance for the realization of metamaterial properties and their applications in a multitude of fields. As preparation technology continues to evolve and innovate, it is anticipated that metamaterial research will yield increasingly remarkable outcomes.

4. Unique properties and application of disordered alloy metamaterials

4.1. MG metamaterials

4.1.1. Mechanical performance of MG metamaterials. Amorphous materials, specifically silicon-based and metal-based glasses, have been observed to exhibit inherent brittleness under tensile stress. Despite this, MGs often demonstrate mechanical properties that outshine those of their crystalline counterparts. The principal obstacle impeding their utilization in engineering contexts, however, is the absence of tensile ductility. Over the last three decades, substantial efforts have been exerted by researchers to devise novel multicomponent alloys and processing methodologies to augment tensile ductility. Three notable examples can be highlighted. Firstly, composition design has been employed to identify new, suitable glass-forming agents within the expansive multicomponent compositional space. Secondly, the advancement of MG composites has taken place. In certain instances, nanocrystalline phases are integrated into a glass matrix [66–68]. While this tactic has proven effective in some systems, it disrupts the intrinsic disordered nature of the matrix as a whole. An alternative approach involves the fabrication of nanoporous MG, which can be interpreted as the introduction of a phase with zero shear modulus into the glass matrix [69, 70]. Lastly, a variety of techniques have been implemented in recent years to rejuvenate the glass state [71]. One such method includes designing a meticulously crafted notch to ascertain the specific properties [72]. Nonetheless, these methods have not yielded significant improvements. Regardless of the specific MG, deformation consistently remains restricted to nanoscale bands that initiate and propagate rapidly, dissipating the input energy. This contrasts with crystalline materials, where multiple plastic carriers collaborate to delay mechanical failure. Achieving tensile ductility in glass requires addressing the issue of deformation localization, which defies conventional wisdom. Consequently, an innovative and effective approach is urgently needed. Interestingly, MGs can display

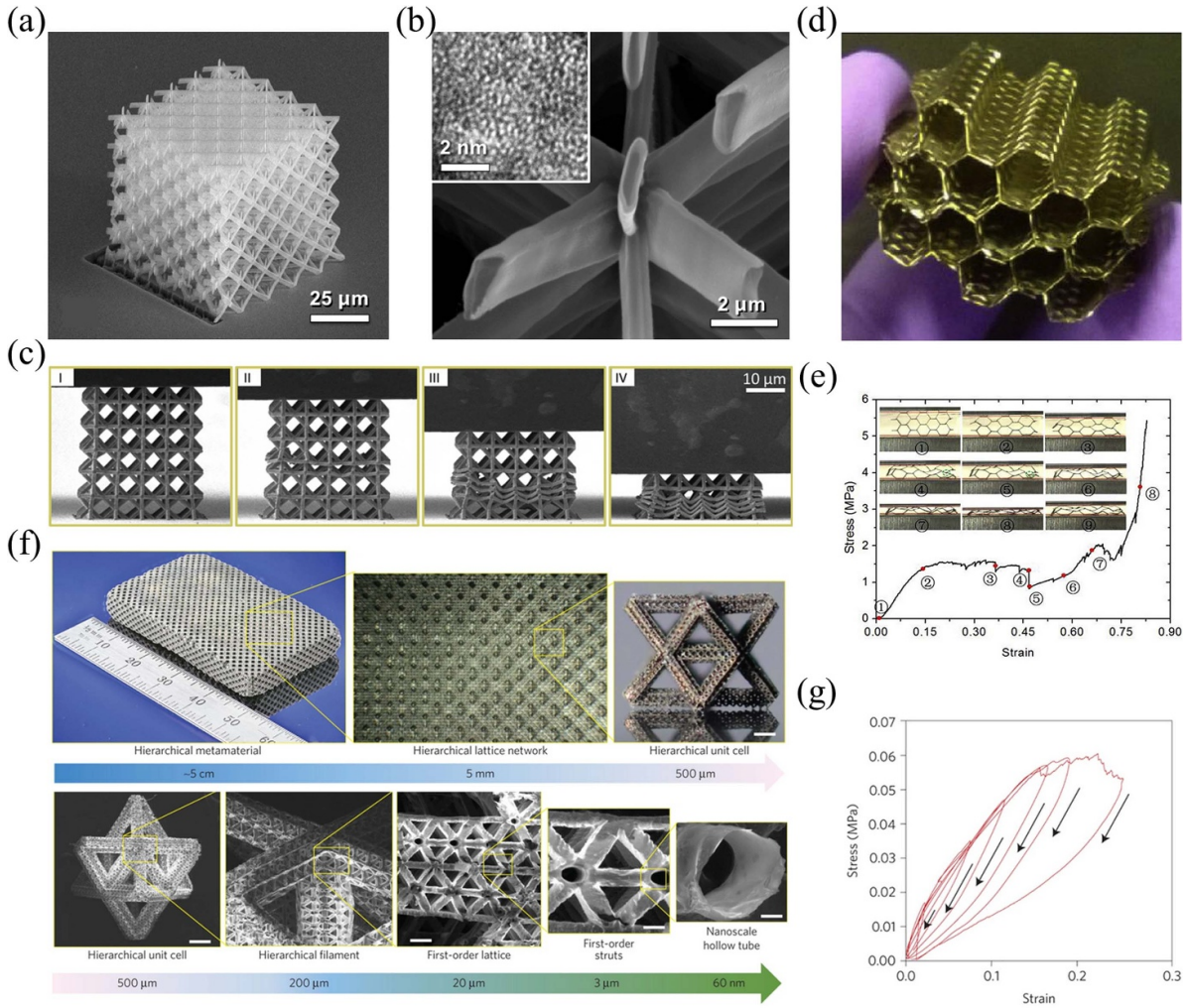

Figure 4. Plasticity and superelasticity of metallic glasses by lattice architect and multiscale design. The SEM images of (a) hollow-tube octet $Cu_{60}Zr_{40}$ nanolattice and (b) the magnified view of hollow lattice members. (a)–(b) Reprinted with permission from [77]. Copyright (2015) American Chemical Society. The inset in (b) is the HRTEM image of atomic configuration. *In-situ* images obtained during compression are shown in (c) (I-IV) for the nanolattice with a wall thickness of 20 nm. Reprinted from [78], © 2017 Acta Materialia Inc. Published by Elsevier Ltd. All rights reserved. (d) Typical honeycomb-like hierarchical $Zr_{35}Ti_{30}Cu_{8.25}Be_{26.75}$ microlattice with dimensions of approximately 3 cm × 3 cm × 2 cm. (e) Quasi-static compression of a 3D honeycomb-like structure with a density of 0.39 g cm^{-3} (or relative density of $\rho/\rho_s = 0.073$) reveals a stress–strain curve that shows high elasticity (∼15%), followed by plastic yielding, and ending with densification. (d)–(e) Reprinted from [79], Copyright © 2015 Acta Materialia Inc. Published by Elsevier Ltd. All rights reserved. (f) Optical microscope images (upper panel) of NiP hierarchical lattice material with a network of hierarchical stretch-dominated octet unit cells. Scale bar in upper panel is 80 μm. SEM (lower panel) displaying the cross-sectional breakdown of the structural hierarchy of the multiscale metamaterial unit cell, revealing details down to wall thicknesses of tens of nanometers. The scale bars in the third and fourth images of the lower panel are 10 μm and 3 μm, respectively. (g) Cyclic tensile stress–strain response of a bend-stretch hierarchical lattice with 60 nm hollow tubes, showing behavior before permanent fracture. (f)–(g) Reproduced from [80], with permission from Springer Nature.

remarkable tensile ductility at the nanoscale [73–75], despite their inherent brittleness under tensile stress. Nanoscale necking becomes apparent, effectively impeding the nucleation and propagation of shear bands. These findings suggest that reducing the characteristic size of MGs to the nanometer scale can mitigate the brittle failure that plagues MG, preventing catastrophic damage during use. Inspired by this phenomenon, the development of 3D MG metamaterials using micro–nano construction techniques may offer an ideal solution to achieve large deformable MGs through nanoarchitecture [76]. This approach involves maintaining the critical dimensions of MGs (such as film thickness) at the nanoscale, without restricting the overall macroscopic size of the structure.

Greer *et al* [77, 78] first fabricated a MG nanolattice using a novel approach. The process began with the creation of a polymer framework through a direct laser-written two-photon lithography technique, developed by Nanoscribe GmbH. Following the magnetron sputtering of MG, the internal polymer framework was exposed using focused ion beam milling, which prepared it for subsequent hydrogen plasma etching. Figure 4(a) displays scanning electron microscope (SEM) images of a $Cu_{60}Zr_{40}$ MG with a wall thickness

of approximately 120 nm. Figure 4(b) depicts hollow components, with high-resolution transmission electron microscope (HRTEM) images confirming the disorder atomic configuration. *In-situ* nanomechanical instruments were employed to conduct *in-situ* compression experiments on the MG microlattices. Figure 4(c) presents a continuous image sequence of *in-situ* compression of MG nanolattices, with a wall thickness of around 20 nm. The images demonstrate the gradual, layer-by-layer collapse and folding of the nanolattices atop one another. Remarkably, the layers fold neatly together without causing catastrophic damage to the nanolattices. The bars stay intact, and the overall structure of the unit cell remains recognizable.

Layer failure in this mechanism consistently begins with the collapse of the beams in the lower half of each cell, while the beams in the upper half of each cell remain largely unaffected throughout the compression process. This behavior may be attributed to the directionality of the sputtered deposition, causing variations in wall thickness and resulting in a thicker beam wall in the upper half of each cell. Consequently, the thinner bottom beams in each unit cell are more prone to deformation compared to their thicker counterparts, leading to a concentration of failures in the bottom beams. Furthermore, Liontas and Greer *et al* [78] identified two transitions in room-temperature deformation patterns: (1) brittle-to-ductile at wall thicknesses between 120 and 60 nm, and (2) plastic-to-elastic at wall thicknesses between 60 and 20 nm. At a reduced temperature of 130 K, the wall thickness changes from 120 and 60 nm to 20 nm, and the deformation mode shifts from brittle failure to elastic buckling without plastic deformation.

The scalability of MG microlattices fabricated through two-photon lithography is constrained. Liu *et al* [79] developed 3D MG honeycomb structures by combining MG sheet patterning based on thermoplastic forming (TPF) with parallel connection technology. This process consists of four primary steps: (1) MG sheet formation, (2) TPF-based MG sheet patterning and perforation, (3) parallel connection, and (4) stripping. The main advantage of this manufacturing method is its compatibility with an air environment and its efficacy for the highly reactive MG, such as zirconium-based alloys. Liu *et al* [79] employed ZrTiCuBe MG, known for its high reactivity, low cost, and easy availability, to fabricate honeycomb structures (figure 4(d)). This approach not only demonstrates the high efficiency of the joining method but also possesses significant practicality for structural applications of MG. Figure 4(e) presents a typical stress–strain curve for a 3D MG honeycomb structure with a relative density of $\rho/\rho_s = 0.073$, where ρ denotes the apparent density of the cellular structure and ρ_s represents the density of the cellular structure's substrate. Distinct deformation behaviors were observed, including elastic deformation ($\sim$15%), plastic yield, and densification. The extended plateau region from $\sim$15% to $\sim$80% is reinforced by plastic deformation. This high plasticity indicates that the 3D MG cellular structure possesses remarkable energy absorption properties [81–84]. Upon unloading, the 3D MG structure is partially restored, and the interface remains intact due to layering (as seen in figure 4(e)). The other three cellular structures with varying relative densities exhibit similar behavior, with larger ρ resulting in higher yield strength and lower elasticity. Consequently, the larger the cell wall length-to-diameter ratio and the lower the relative density, the easier the transition from linear elasticity to nonlinear elasticity (or elastic buckling). The superior deformability of 3D cellular structures, combined with their high strength, endows them with exceptional elastic energy storage capabilities. These properties make them superior to structures made from other materials, such as metals and ceramics.

Natural materials such as wood, pearl, diatoms, and bone have evolved through strategies that organize 3D structures from the nanoscale to the macroscale, often spanning sizes across at least five orders of magnitude [85]. Modern imaging and analysis tools reveal that these materials exhibit ordered structures across multiple length scales, with each hierarchical level contributing equally to the properties of the bulk material [86, 87]. For instance, bone trabeculae, which have been extensively studied, contains a layered arrangement of cellular structures distributed over seven orders of magnitude on a length scale. This arrangement enables them to achieve high strength and fracture toughness with minimal weight [88]. The centimeter-scale porous structure is composed of a network of ligaments, each containing a complex structure consisting of a microstructured hollow fiber network of concentric lamellae at the submicron scale. Gecko toes possess an extraordinary adhesive system, featuring a multi-layered structure of fibers that break down into finer filaments down to the nanoscale [89]. Recent modeling and experimental work have demonstrated that mechanical properties can be enhanced by introducing structural layers into the topological framework of 3D architectures [90, 91]. However, the structural span is confined to fractal features within three orders of magnitude, with a maximum size of a few hundred microns. The impact on macroscopic properties at a global scale is still largely unexplored. Zheng *et al* [80] proposed a new approach to multiscale metamaterial design by assembling microscale filaments along a structurally defined path at a higher length scale. This approach enables the assembly of a wide range of micro-architectures, each with distinct deformation mechanisms at various length scales, into larger objects with adjustable properties. At each level, the orientation, relative density, mosaic, and feature size of the cells are parameterized and designed to iteratively form a block-scale lattice in three dimensions. The creation of this scalable metamaterial is made possible by a novel AM technique called Large Area Projection Microstereolithography (LAPμSL). This technique integrates an addressable spatial light modulator (SLM) with a synchronized optical scanning system to fabricate microscale structures over a larger processing area. It utilizes a galvanometer coupled with a custom scanning lens to project the light pattern from the SLM onto the surface of the UV-cured monomer. As the light is scanned, the image projected by the SLM changes, creating arbitrary patterns anywhere on the liquid surface and producing miniature features with a feature size range spanning more than four orders of magnitude. A thin layer of nickel–phosphorus metal–glass (MG) is deposited onto the base diacrylate polymer layered

metamaterial created by LAPμSL through electroless nickel plating. After the nickel shell reaches the desired thickness, the polymer structure is chemically removed, leaving behind tubes with thicknesses ranging from 50 nm to 700 nm. This technology enables the creation of miniaturized architecture on a large area combined with nanoscale post-processing. At the macroscopic scale ($\sim$5 cm) (figure 4(f)), the MG metamaterial comprises octahedron–tetrahedral (octet) cells dominated by layered tension, which are designed to bear loads by axial stress (figure 4(f)). Each tensile master cell in the layered lattice network shown in figure 4(f) contains approximately 200 μm layered support elements. These consist of a network of tensile master cells organized in a (110) direction. These master cells are composed of micro-thin-walled hollow nickel–phosphorus tubes. At the lowest level, these materials consist of thin-walled hollow nickel–phosphorus tubes with a thickness ranging from 50 to 700 nm. The layered nature of the material in figure 4(f) reveals an arbitrary 3D nanostructured material with an overall macroscale size. This multiscale MG metamaterial, with its combined layered topology, exhibits remarkable mechanical behavior at the macroscopic scale. The bulk layered bend-tensile metamaterial with a wall thickness of 60 nm displays a maximum elastic limit of over 20% (figure 4(g)), a value surmounting low-density metal alloys or nanolattices [92]. These lattices have been noted for their ability to stretch elastically in a reversible manner after several loading cycles, before reaching a point of breakdown. This impressive elasticity can be credited to the successive rotation of flexible, layered ligaments, initial node rotations, and stretching of hollow tubes with nanoscale wall thicknesses. When subjected to pulling forces, the layered ligaments, governed by second-order bending, rotate around their nodes, effectively unfolding from their original position. As the force increases, more hollow tube struts of the first order rotate around their nodes, eventually reaching an angle close to 90° relative to the horizontal, and continue to stretch. When strains surpass the hollow tube's elastic limit, microscopic damage occurs at the nodes of the primary strut, leading to the breakdown of the node and, ultimately, the secondary structure's failure. This damage culminates in the material's tensile failure. The combined rotation of the elastic hinge at the nanoscale node and the second-order layered column produces a superelastic strain, a characteristic not commonly seen in materials composed of brittle metal glass.

This method can be leveraged for an extensive range of metamaterial property designs. By employing a blend of deformation-dominated microstructures at varying continuous lengths, it is possible to achieve unique property combinations that are not typically observed in bulk materials. This makes it possible to exploit nanoscale material properties in larger objects, thereby opening up a broad range of potential applications for these mechanical metamaterials. Note that, SLM enables the precise production of personalized or customized metal products without the additional cost, time or waste associated with traditional plastic processing. One of the main challenges with SLM is the porosity that can occur during the melting process. This can lead to voids or defects in the final product, which can affect the mechanical properties of metal parts and often require significant post-processing, including heat treatment, to remove stress and improve properties. In addition, not all materials are suitable for SLM, such as highly reflective materials like copper. The unique layer-by-layer cyclic heating of SLM processing has always induced *in situ* crystallization in MG.

4.1.2. Functional application of MG metamaterials. Beyond their superior mechanical attributes, MGs possess distinct functional characteristics which include, but are not limited to, catalytic properties, biocompatibility, resistance to corrosion and wear, optical properties, energy absorption capacity, soft magnetic properties, and magnetothermal effects [67, 93, 94]. The functional properties of these alloys can be further augmented by fabricating glass components with a 3D lattice structure.

Yang *et al* [95] have fabricated Zr-based MG lattices of varying geometric shapes, inclusive of cube, hollow, and lattice structures, utilizing SLM and dealloying techniques. As depicted in figure 5(a), the degradation efficiency of an amorphous alloy lattice for methyl orange (MO) is compared with a cubic sample (identical dealloying procedure) and a polycrystalline copper plate under identical conditions. Significantly, the lattice sample demonstrated a much higher degradation rate, completely removing MO in under 15 min. This is roughly four times more efficient than the cubic sample and nine times more efficient than polycrystalline copper. Furthermore, the lattice structure with the maximum degradation rate demonstrated commendable stability during cyclic degradation; the degradation efficiency did not markedly diminish after four cycles (figure 5(b)), suggesting the material's high catalytic stability. The mechanism adheres to the classical advanced Fenton process [96, 97]. The 3D bulk catalyst possesses a hierarchical porous structure. The surface of Cu interacts with H_2O_2, generating hydroxyl radicals (HO–), which function as potent oxidants that react with the dye, resulting in dye decolorization. The lattice sample's catalytic performance surpasses that of other samples, primarily due to its expansive surface area and hierarchical porous structure. To elucidate the surface areas of distinct geometries, nanoporous layers from different MG samples (cubes and lattices) were removed and subsequently analyzed through Brunauer–Emmett–Teller (BET) measurements, revealing a specific surface area of approximately 10 $m^2\ g^{-1}$. In the degradation experiments using the equivalent mass (27.2 g l^{-1}) for the three 3D printed samples, the lattice samples displayed the largest surface area (25 m^2), which was nearly 3 times greater than the hollow samples and 19 times greater than the cube samples, as shown in figure 5(c). The substantial reaction surface area, coupled with the micron/nanometer fractured porous structure, not only supplies more catalyst and exposes the most active sites (e.g. edges and surfaces surrounding the pores) [98], but also demonstrates a robust adsorption effect on dye molecules. Additionally, it facilitates the complete transfer of H_2O and easy removal of by-products generated during the degradation process, thereby promoting subsequent degradation reactions.

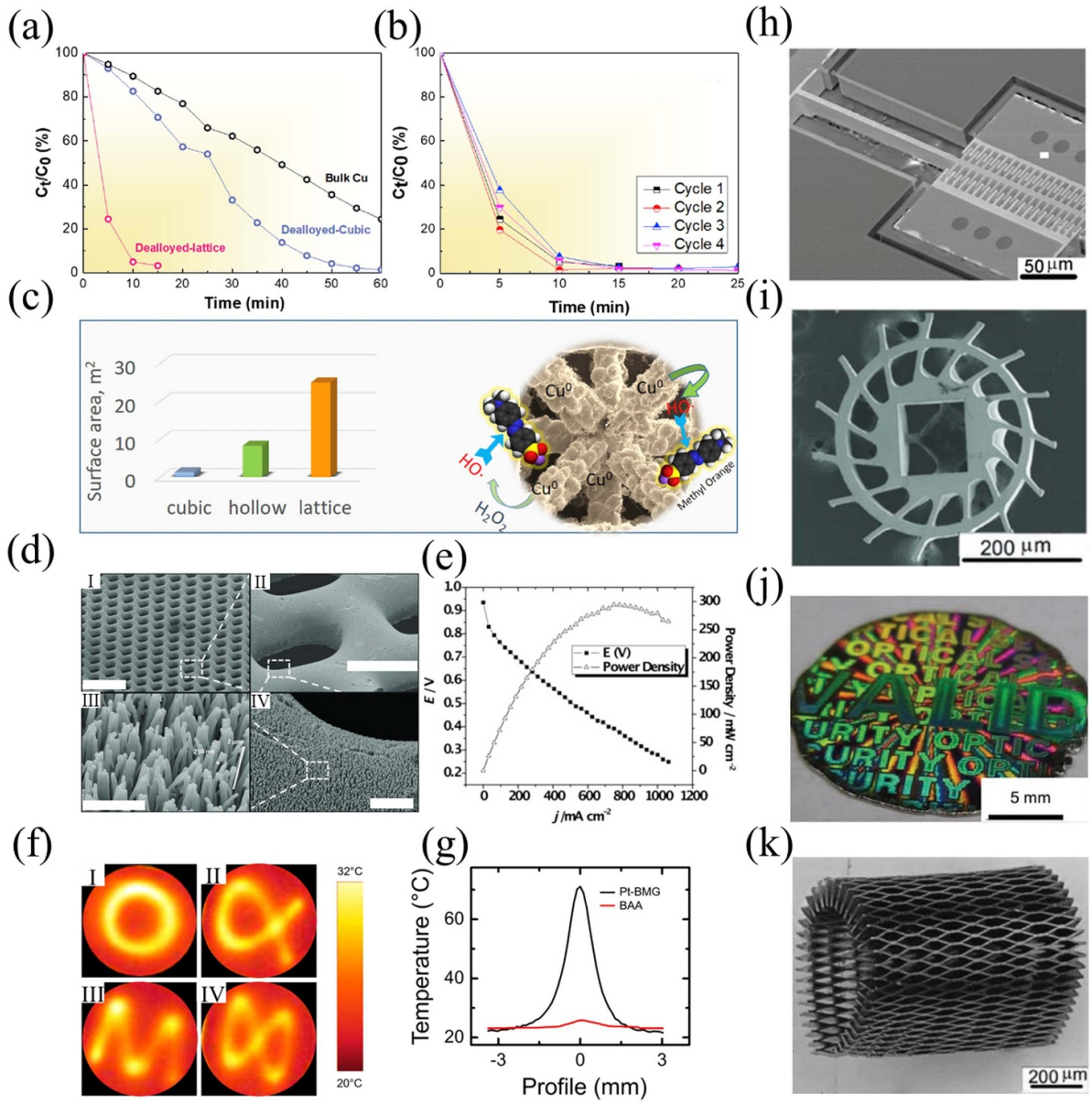

Figure 5. Functionality of metallic glass metamaterials. (a) Degradation rate as a function of time for the 3D-printed metallic glass cubic and lattice samples with a nanoporous surface, compared to a polycrystalline Cu. (b) The cycling stability of the dealloyed lattice sample. (c) The surface area of the 3D-printed BMG components (left panel) with various geometries under equivalent sample mass and (right panel) schematic illustration of the benefit of the hierarchical architect in the degradation of methyl orange. (a)–(c) Reprinted from [95], © 2017 Elsevier Ltd. All rights reserved. (d) SEM images of the finished Pt-based MG nanowire electrode with gas feeding through-holes. (e) Fuel cell polarization curve of Zr-based MG flow field with standard Pt/C ETEK (0.5 mg_{Pt} cm^{-2} loading). (d)–(e) [99] John Wiley & Sons. Copyright © 2013 WILEY-VCH Verlag GmbH & Co. KGaA, Weinheim. (f) Thermal images of several Lissajous patterns configured onto Pt-based MG metamaterials. $A_1 = A_2 = 0.2$ V (I) $m = n = 1$, $\varepsilon = \pi/2$, $P = 2.3$ W mm^{-2}; (II) $m = 2$ $n = 3$, $\varepsilon = \pi/4$, $P = 2.5$ W mm^{-2}; (III) $m = 1$ $n = 4$, $\varepsilon = 3\pi/8$, $P = 2.3$ W mm^{-2} and (IV) $m = 1$ $n = 2$, $\varepsilon = 0$, $P = 2.2$ W mm^{-2}. (g) Horizontal temperature line profiles of thermal images for Photo-induced-heat localization on MG metamaterials. (f)–(g) Reprinted from [100], with the permission of AIP Publishing. (h) A linear $Pt_{57.5}Cu_{14.7}Ni_{5.3}P_{22.5}$ MG comb-drive actuators. The comb teeth measure 5 μm in width and 20 μm in length. When an alternating current (AC) voltage is applied, the combs are set into motion. (i) A $Zr_{35}Ti_{30}Cu_{8.25}Be_{26.75}$ microgears fabricated by micromolding techniques using silicon molds. (j) A $Au_{49}Ag_{5.5}Pd_{2.3}Cu_{26.9}Si_{16.3}$ MG metasurface, which mimics the nickel master mold, is imprinted into $Au_{49}Ag_{5.5}Pd_{2.3}Cu_{26.9}Si_{16.3}$ BMG. The dispersion of white light into various colors demonstrates the precision with which the master mold pattern has been replicated in the MGs. (k) Stent fabricated by rolling a $Pt_{57.5}Cu_{14.7}Ni_{5.3}P_{22.5}$ MG lattice into a cylindrical shape. (h)–(k) [74] John Wiley & Sons. Copyright © 2011 WILEY-VCH Verlag GmbH & Co. KGaA, Weinheim.

A layered superstructure fabricated from thermoplastic-based $Pt_{57.5}Cu_{14.7}Ni_{5.3}P_{22.5}$ MG, serving as a high surface area catalyst and porous gas diffusion layer, represents a promising candidate for micro fuel cells, as reported by Sekol *et al* [99]. The MG lattice electrode features uniformly distributed pores on its surface, with a pore size and spacing of 110 μm. The pore spaces are embellished with nanowires of 250 nm, which in turn contribute to a surface area of 0.16 cm^2 (figure 5(d)).

SEM images confirm that the shape and distribution of these nanowires are unaffected by subsequent embossing on the silicon mold. As a result, this fabrication method provides the potential to pattern layered structures spanning three orders of magnitude. It also enables the independent customization of porosity and catalytic surface area in two distinct processing stages. The active surface area can be increased by lengthening and/or reducing the diameter of the nanowires, while adjustments to the porosity can be made by changing the diameter or spacing of the microcolumns in the silicon mold. Standard Pt/C inks (ETEK) applied on a gas diffusion layer were employed to gauge the performance of the Zr-based MG flow field electrodes and the all-encompassing MFC designs. Figure 5(e) illustrates the polarization curve of a standard catalyst with a room temperature power density of 294 mW cm^{-2} and a platinum load of 0.5 mg cm^{-2}. This represents an enhancement over the optimal power density of 194.3 mW cm^{-2}, achieved when the flow field is composed of a gold-sputtered silicon wafer with a Pt/C catalyst layer [101]. This is the first functional Proton Exchange Membrane micro fuel cell, where the components of the catalytic and gas flow field consist of a complex layered MG microlattice that encompasses features of both nanometer and micron sizes.

Materials with high optical-to-thermal energy conversion efficiency are essential for renewable energy applications. Optical excitation can effectively generate controlled, localized heat at relatively low excitation light power. However, challenges such as transverse heat diffusion into the surrounding illuminated area and the resulting low photothermal energy conversion efficiency persist for metal surfaces. Surface nanoengineering has proven to be effective in enhancing heat absorption and generation. According to Uzen *et al* [100], MG microlattice is used to achieve noticeable spatial thermal localization and high temperature. As shown in figure 5(g), although the two samples display similar absorption at $\lambda = 980$ nm, the photoinduced temperature distribution and maximum temperature reached are significantly different. In the laser-irradiated region, clear spatial thermal localization was observed in the Pt-based MG samples, with a maximum temperature of ∼71 °C in the center of the hot spot region. In contrast, BAA samples had a maximum temperature of ∼26 °C, only slightly above room temperature, with no significant spatial thermal localization observed. The corresponding half-maximum full widths obtained from the horizontal temperature profile along the photoinduced hot spot are ∼1.1 mm and ∼1.3 mm, respectively (see figure 5(g)). In both cases, the width of the hot spot on the sample surface is wider than the incident laser beam, indicating lateral thermal diffusion. One potential application of thermal imaging involves steganography, in which permanent or erasable information is 'hidden' on the surface of an object, undetectable by the human eye or a traditional CCD camera, but visible to a thermal imager. In practice, this can be accomplished by generating localized spatial heat on the surface of an object to create a well-defined feature. Figure 5(f) provides an example of four photoinduced Lissajous thermal profiles obtained from the surface of the same Pt-based MG sample. These profiles are derived by applying sinusoidal waves to two mirrors, defined by the well-known parametric relationships $X(t) = A1\cos(2\pi f1t + \phi1)$ and $Y(t) = A2\cos(2\pi f2t + \phi2)$, where $A1$ and $A2$ represent the amplitudes, $f1$ and $f2$ are the time frequencies, and $\phi1$ and $\phi2$ are the phase angles of the waveform. As depicted in figure 5(f), $f1 = m \times f$ and $f2 = n \times f$, where m and n are integers ($\geqslant 1$), $f = 50$ Hz, and the relative angular phase shift between the two waveforms ($\varepsilon = \phi1 - \phi2$) differs. The elevated temperatures at the edge of the Lissajous figure are artifacts from the measurements associated with the dynamic response of the galvo mirror. The clear photoinduced image shown in figure 5(f) emphasizes the potential of using Pt-based MG for steganographic applications. This method offers advantages, including the need for only moderate illumination power while preserving a distinct temperature contrast and a defined photothermal positioning between the illuminated and unilluminated regions.

By integrating microforming with planarisation methods, 3D MG microparts of varying complexity and shape, spanning multiple length scales, can be directly produced. Examples of these shapes produced through MG microforming are given in figures 5(h)–(k) [74]. Contrary to parts produced by micromachining, micromolding yields highly precise shapes without any burrs. Consequently, these parts can be directly used in the fabrication of micromachines and similar constructs, without the need for further processing like deburring or polishing. Mesh compression, tensile, and wavy structures can be fabricated for mechanical characterization. Figure 5(h) shows an SEM image of an amorphous alloy linear comb actuator, where the silicon is selectively etched to expose the MG comb actuator, with one end still anchored to the silicon wafer. When an AC voltage is applied to the comb, it generates an electrostatic force between the combs, causing them to either attract or repel depending on the polarity of the voltage. Incorporating springs, levers, or cranks to the comb can convert the linear displacement caused by electrostatic forces into rotation or other motion, achieving a displacement significantly larger than that offered by traditional MEMS materials. The MG micro gear (figure 5(i)) offers numerous advantages such as zero backlash, high repeatability, extended life, and compact design. Moreover, MG micro gears possess superior mechanical properties and enhanced wear resistance [102]. They can find application in watches, micro-actuators, micromanipulators, and micro-harmonic drives. Additionally, MG brackets (figure 5(k)) can be elastically loaded up to 2% strain, significantly reducing the risk of restenosis.

Metamaterials are advancing towards integrated applications. Recently, Lee *et al* [103] demonstrated innovative fabrication of highly transparent supercapacitors (SCs) and electrodes achieved by incorporating MG microarrays into wirelessly rechargeable and nearly invisible skin-heating patches. Electrohydrodynamic jet printing technology is employed to print transparent SCs with fine conductive patterns. Wireless operation is a crucial feature for enhancing the user experience of wearable electronics, particularly for devices that can be attached to the skin [104]. Figure 6 showcases the fabrication process, electrical properties, and working mechanism of a transparent heat patch combined with a wireless functional circuit. The device consists of three main electronic

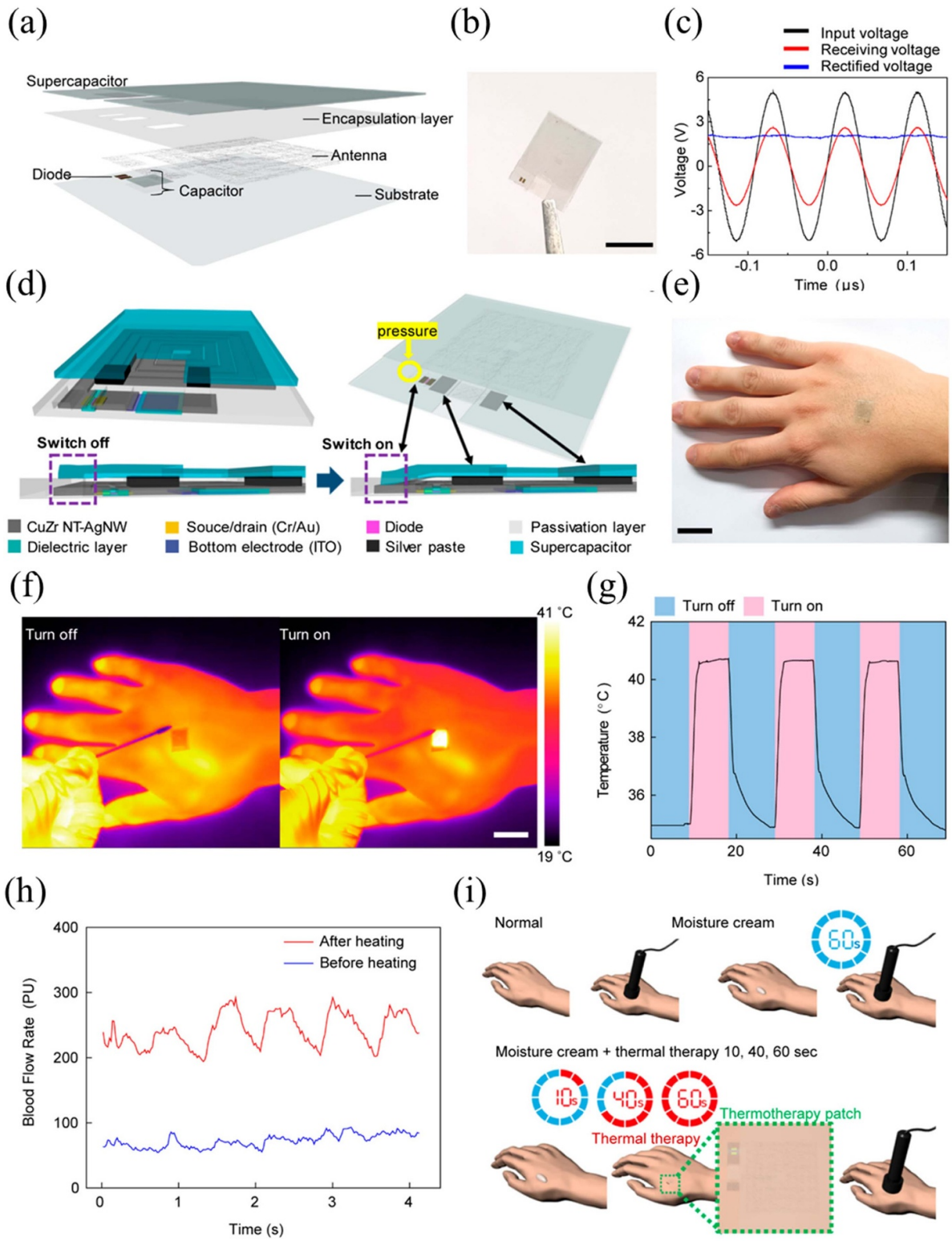

Figure 6. Thermal therapy device application integrated of metallic glass metamaterials. (a) Diagram of the integrated system, comprising a rectifier (diode and capacitor), antenna, and supercapacitor. (b) Image of a wirelessly rechargeable, transparent, and flexible heat patch. Scale bar: 1 cm. (c) Rectification characteristics of the manufactured rectifier. (d) Illustration of the operating mechanisms of the switch and heat patch under applied external pressure. (e) Photograph showing the heat patch attached to the back of a hand. Scale bar: 2 cm. (f) Infrared image of the heat patch with the switch toggled on and off. Scale bar: 2 cm. (g) Thermal stability and on/off performance of the heat patch tested with a single charge. (h) Laser Doppler perfusion monitoring results at a specific skin location, expressed in perfusion units (PU). (i) Diagram depicting hydration state measurements over time during thermal therapy application. (a)–(i) Reprinted with permission from [103]. Copyright (2020) American Chemical Society.

components: a rectifier, an antenna, and a SC, as shown in figure 6(a). The transparent heat patch is developed by seamlessly integrating the antenna, rectifier, and SC, as illustrated in figure 6(b). Except for the silicon diodes, all components of the device are fabricated from transparent materials to maximize transparency. Figure 6(c) illustrates the rectification properties of a wireless power transmission unit, which includes an antenna and a rectifier component. The rectifier circuit is constructed with an ultra-thin 200 nm silicon nanofilm and a P-type Intrinsic/N-type (PIN) diode integrated with SiO2-based capacitors. In this configuration, the antenna wirelessly detects the incoming power, represented by the black line in figure 6(c). The rectifier circuit converts an AC bias of 5.2 peak voltage (V_{pp}) at 13.6 MHz (red line in figure 6(c)) to a DC bias of 2.01 root mean square voltage (V_{rms}) (blue line in figure 6(c)). Figure 6(d) demonstrates the operation of the switch under external pressure. The schematic shows that the transmission circuit is linked to the SC using silver paste, while the switch remains disconnected from the SC electrodes in its default state. When pressure is applied to the switch, it establishes contact with the SC electrodes, allowing the energy stored in the SC to power the antenna for heating. This physical connection between the electrodes activates the switch, enabling the operation of the heat patch. To measure the minimum tactile pressure required to turn on a switch, a commercially available programmable compression tester was used to apply gradually increasing tactile pressure to the device. The heat patch is applied to the back of the hand, showcasing its ability to adhere to the skin (figure 6(e)). It wirelessly receives inductively coupled AC power from a transmitter coil operating at 13.6 MHz, with a transmission range of 10 mm. Figure 6(F) presents infrared images taken before and after activating the switch. When the switch is pressed, the heat sink starts generating heat, causing the heater temperature to rise and stabilize at the target level within 3 s. All on/off functionality tests were conducted using a single charge. For three of the tests, the temperature remained constant at around 40.6 °C (figure 6(g)). Therefore, there is no need to worry about low-temperature burns (>45 °C) caused by the heater. Hyperthermia is one of the most popular physiotherapeutic methods, which can effectively promote blood circulation and reduce inflammation and pain [105]. In addition, heat therapy enhances transdermal molecular movement, thereby increasing the skin permeability of the drug [106]. Here, blood flow and skin hydration rates were measured to demonstrate the effectiveness of the heat patch. First, one of the effects of hyperthermia, increased blood flow due to telangiectasia, was measured using a laser Doppler imaging (LDI) device [107]. Figure 6(h) shows the results of laser Doppler perfusion monitoring at a point in the skin. The measurements are expressed in perfusion units (PU), which is arbitrary [108]. Compared to before hyperthermia, blood flow in skin heated for 1 min (41 °C) was 3.8 times higher than in normal skin. Figure 6(i) presents a schematic of the mechanism of measuring skin moisture changes to demonstrate the effectiveness of heat therapy.

4.2. H/MEA metamaterials

4.2.1. Mechanical performance of H/MEA metamaterials.

As a breakthrough of traditional design strategy, high/medium entropy alloy can dramatically expand the composition space and precisely tune the microstructure to achieve outstanding mechanical and unique functional properties. For instance, CrMnFeCoNi was reported to be one of the toughest materials to date at both room and cryogenic temperature [109]. Therefore, combining the advantages of topology design of metamaterials and optimized composition, high/medium entropy alloy metamaterials becoming an attractive region in terms of mechanical and functional applications.

The advent of HEA in materials science has transformed alloy design strategies from relying on a single principal element to employing multiple principal elements. This shift has resulted in advanced materials with unique properties, such as high strength combined with sufficient ductility, fracture toughness, and excellent corrosion resistance across a wide temperature range. The mechanical properties of HEAs are greatly influenced by their compositions and microstructures. The compositions determine the elastic characteristics and atomic-scale interactions with dislocation activity, thus influence the mechanical response. Microstructure is significantly dependent on their synthesis process and post-treatment parameters. The topological design of metamaterials introduces third dimensions to participate in the modulation of mechanical properties. Extrusion-based 3D printing is one of the most common printing techniques [110]. Through 3D extrusion printing of inks containing a blend of Co_3O_4 + Cr_2O_3 + Fe_2O_3 + NiO nanometric powders and followed by co-reduction to metals, a single-phase fcc HEAs FeCoNiCr microlattice was successfully fabricated (figure 7(a)). Fully annealed FeCoNiCr microlattice exhibited 99.6 ± 0.1% with the resolution down to 100 μm relative density excellent mechanical properties at ambient and cryogenic temperatures [50]. During the compressive deformation of microlattices, the lattices exhibit no evidence of catastrophic cracking or sudden strength loss even when subjected to compaction beyond 50% strain, demonstrating their exceptional energy absorption capacity. Similarly, 3D-architected CoCrFeNiMn microlattices were fabricated using direct ink writing (DIW) combined with thermal sintering in figure 7(b), showing remarkable specific energy absorption of 54–63 J g^{-1} [111]. Laser powder bed fusion process is another commercial and mostly widely used fabrication strategy, which can fabricate various high-entropy alloy lattice structure with unprecedent design freedom, for example the previously reported eutectic high-entropy alloy lattice structure in figure 7(c) [112]. Besides, some unique strategies for fabricating the core-shell medium/high-entropy alloy micro/nanolattice are emerging. Magnetron sputtering based deposition method is the most common and effective way to fabricate the HEA thin film. Therefore, a core-shell HEA lattice structure composites at nanometer scale

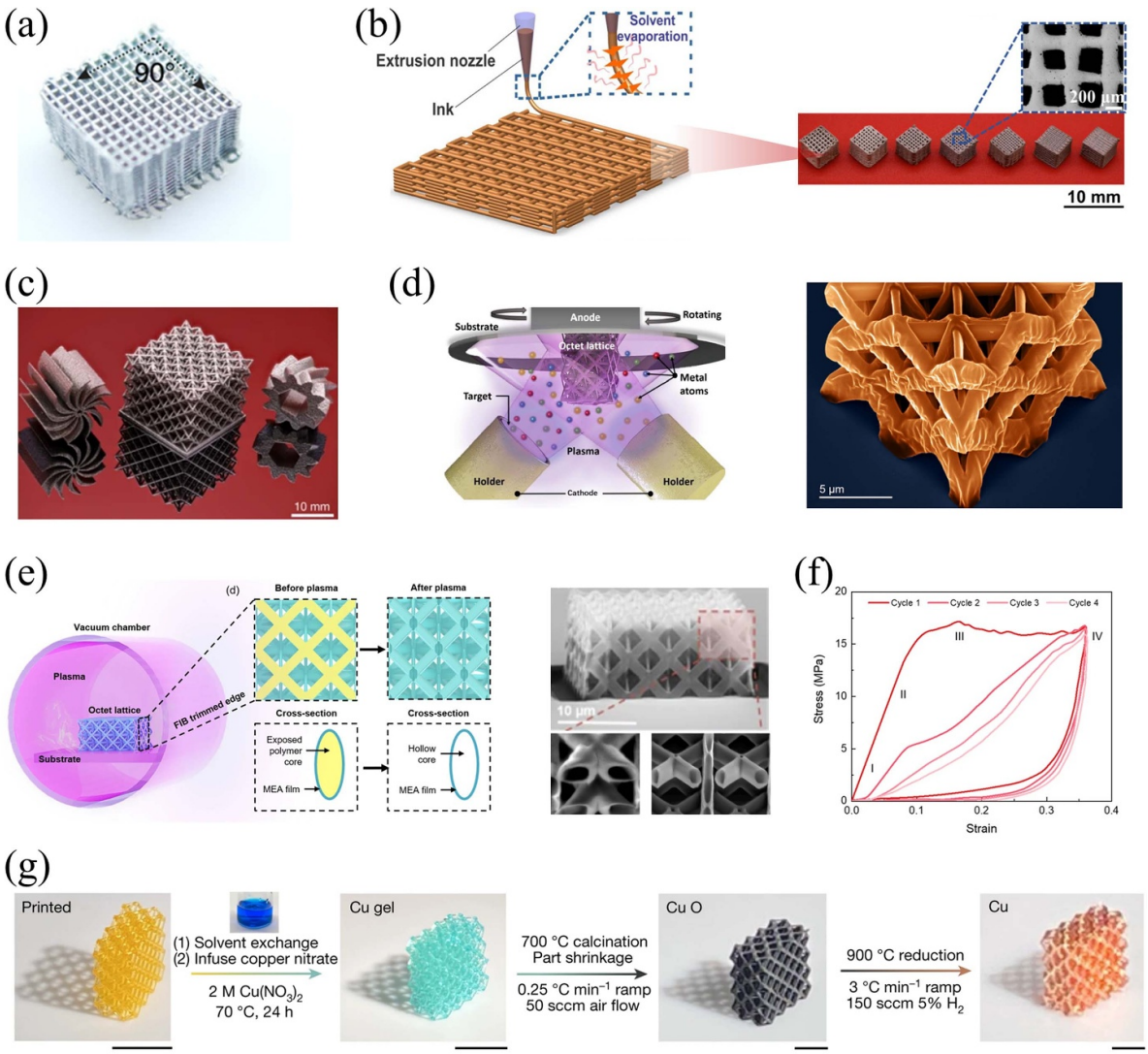

Figure 7. Fabrication strategies and mechanical properties of HEA/MEA metamaterials. (a) Fabrication of CoCrFeNi high-entropy alloys via 3D ink-extrusion, reduction, and sintering. (b) CoCrFeNiMn microlattice via direct ink writing (DIW) combined with thermal sintering process. (a)–(b) Reprinted from [111], © 2020 Acta Materialia Inc. Published by Elsevier Ltd. All rights reserved. (c) Eutectic high-entropy alloys octet-truss microlattice fabricated by laser powder bed fusion process. Reproduced from [112], with permission from Springer Nature. (d) Fabrication process of the CoCrNiTi-coated core–shell nanolattice. (e) Fabrication process of hollow MEA nanolattices. (f) Mechanical characterization of hollow MEA nanolattices. (d)–(f) Reprinted from [113], © 2020 Elsevier Ltd. All rights reserved. (g) Hydrogel infusion additive manufacturing technology and fabricated FeCoNiCu HEA microlattices. Reproduced from [115], with permission from Springer Nature. The scale bars in g are 5 mm, 5 mm, 1 mm, and 1 mm from left to right respectively.

were developed combining the two-photon lithography direct laser writing and magnetron sputtering deposition technologies (figure 7(d)). Specifically, in 2021, Feng *et al* [113] reported a microalloyed medium-entropy alloy (MEA) $CoCrNiTi_{0.1}$ thin film with extra low stacking fault energy. Their fabricated MEA-coated nanolattice can display unprecedented surface wrinkling phenomenon during compression experiment, leading to the remarkable specific strength and unparalleled toughness at strains over 50% and up to 60 MJ m^{-3} energy absorption capacity (figure 7(d)). Furthermore, the hollow CoCrNi MEA nanolattices were developed via the two-photo technology and subsequent plasma etching treatment (figure 7(e)), which displayed superior specific energy absorption (up to 25 J g^{-1}) and over 90% recoverability due to the high toughness of MEA composition design (figure 7(f)). The superior strength and resilience can be contributed to the size effect-induced ductility and high-density material crystal defect [114]. Recently, a novel AM technology of micro-architected HEA was proposed through infusing the 3D-architected hydrogels with HEA precursors [115], then calcining and reducing to pure HEA microlattices (figure 7(g)). They employed this technique to successfully a series of normal alloy and HEA microlattices, including the Cu and FeCoNiCu HEA.

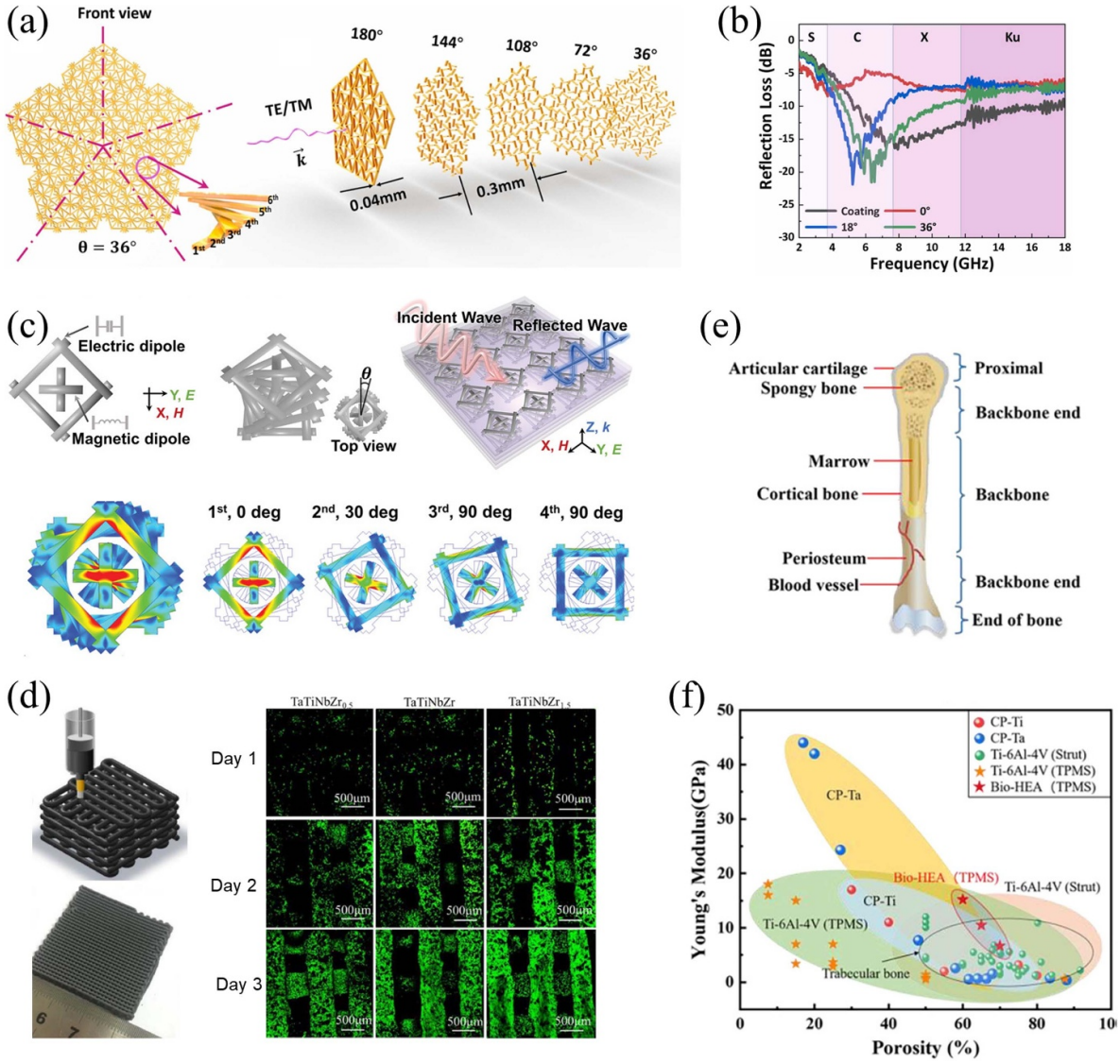

Figure 8. Functionality of HEA metamaterials. (a) Stereogram of FeCoNiSiAl high entropy alloy quasiperiodic-metamaterials along with Penrose tiling twisted 36°. (b) The reflection loss of coating and metamaterials with robust absorption. (a)–(b) Reprinted from [116], © 2023 Elsevier B.V. All rights reserved. (c) Design diagrams of the unit of chiral metamaterials, and its microwave-absorbing property from finite element analysis results [117] John Wiley & Sons.© 2022 Wiley-VCH GmbH. (d) Fabrication process of porous bio high entropy alloy metamaterials, and fluorescence images of MC3T3-E1 cells cultured on TiZrNbTa metamaterials. Reprinted from [118], © 2023 Published by Elsevier Ltd on behalf of The editorial office of Journal of Materials Science & Technology. (e) Diagram of human bone structure. (f) Young's modulus comparison of TPMS high entropy alloy metamaterials with that of human bone and other porous biomaterials. (e)–(f) Reprinted from [119], © 2022 The Society of Manufacturing Engineers. Published by Elsevier Ltd. All rights reserved.

4.2.2. Functional application of H/MEA metamaterials. Due to the broad composition design space, HEAs-based metamaterials exhibit abundant multifunctional applications. In term of electromagnetic metamaterials, Ma *et al* [116]designed cascaded quasiperiodic metamaterials using $FeCoNiSi_{0.3}Al_{0.3}$ HEAs ribbon (figure 8(a)) with high conductivity and soft magnetic performance. The metamaterials derived from quasiperiodic structures, which form asymmetric patterns, achieve an effective absorption bandwidth of 3.8–18 GHz within a thickness of 5.1 mm. By steering the wavefront vector of electromagnetic waves, the bulk size can be reduced, enhancing effectiveness and promoting the development of high-performance absorbers in the low-frequency range of 2–18 GHz. Similarly, inspired by the epidermal ordered structure arrangement of jeweled beetles, Shi *et al* [117] developed a chiral metamaterial consisting of consisting of HEA electromagnetic dissipative unit and media-layer (figure 8(c)), exhibiting superior absorption with effective absorption bandwidth of 4.48 GHz at 2 mm interlayer medium thickness and minimum reflection loss of −53.6 dB. Attributing to the development of the nontoxic biological HEA system, HEA metamaterials also exhibit the promising potential on the implants used to repair bone defects. Based on the DIW 3D printing technology, a porous TaTiNbZr

bioHEA scaffold was developed using four metal powders as composite ink (figure 8(d)). Metamaterial exhibits a tunable compressive strength of 70.08–149.95 MPa and an elastic modulus of 0.18–0.64 GPa [118]. The $TaTiNbZr_{1.5}$ scaffold exhibited the most favorable biological properties among the porous bioHEA scaffolds studied, which were close to those of a porous Ta scaffold. In addition, Feng *et al* [119] utilized the SLM technique to fabricate the $Ti_{1.5}NbTa_{0.5}ZrMo_{0.5}$ HEA triply periodic minimal surface (TPMS) lattice structure. They have Young's modulus ranging from 6.71 to16.21 GPa, which is very close to that of human trabecular bone (figure 8(f)). HEA metamaterials show the possibility for various bone implants by customizing the topology and porosity of the TPMS lattice to meet the mechanical and biocompatibility requirement.

5. Conclusion

In summary, this review provides a comprehensive analysis of the current state of research in the rapidly evolving field of metamaterials. The advancement of fabrication technologies has led to the emergence of 3D disordered alloys metamaterials, including MG and high/MEA metamaterials, which have established a novel paradigm for the interplay between structural and functional properties. This has the potential to transform diverse scientific disciplines such as photonics, acoustics, and electronics. The introduction of the lattice concept enables MGs and HEAs to exhibit excellent properties, including superelasticity, which differ from those of traditional bulk materials. The systematic exploration and progress in the realm of 3D disordered alloy metamaterials have the potential to have a significant impact on the future trajectory of materials science, engineering, and technology. As our comprehension of these materials deepens, the subsequent innovations in topology design, dynamic mechanical performance, and reconfigurable response are poised to revolutionize the manner in which materials are tailored for a wide array of integrated applications. Ultimately, this review serves as a crucial resource that not only highlights the significance of 3D disordered alloy metamaterials but also underscores the importance of continued research in this interdisciplinary field.

6. Future perspectives

After two decades of rapid advancement, mechanical metamaterials are emerging as a unique platform for creating integral components by combining topological design and innovative materials, with the goal of proactively achieving specified functionalities. Despite the significant progress in this field, numerous breakthroughs remain to be made to advance the industrial application of mechanical metamaterials across various sectors.

Topology design: Conventionally, the generation of topology optimization for lattice structures typically relies on an extensive series of computationally demanding finite element analyses. The recent progress in software and data-driven modeling methods can significantly improve the efficiency of topological optimization of architected materials. Typically, due to the introduction of the fast prediction of neural networks, the consideration of only a few initial design parameters for lattice structures can output an infinitely large design space. Integration of data-driven approaches with topology optimization allows the researchers to efficiently design complex and hierarchical lattices with minimal computational cost, providing promising potential to customize various mechanical response and functional applications.

Mechanical response: As of now, tremendous effort has been put to address the quasi-static behavior of the various metallic architected materials at ambient temperature. However, given the potential applications in aerospace and defense industries, metallic architected materials must endure more complex and challenging working conditions, including but not limited to high-speed impact, high/cryogenic temperature deformation, and fatigue. For instance, it is widely acknowledged that elevated temperatures adversely affect the mechanical integrity of nearly all metal alloys. In this circumstance, it is necessary to develop the new metallic lattice structure with outstanding microstructural stability and resistance to softening for high-temperature applications. However, there are currently few studies on the lattice topology-level structure design and inherent microstructural design that serve under extreme load conditions. In comparison to conventional bulk materials, architected metallic materials incorporate the topology structure factor, which can potentially influence their microstructural evolution route and interaction behavior of various defect types, such as the dislocation, deformation twins, and phase transformation. Typically, Octet lattices experience deformations dominated by stretching under external loads, with the loads primarily being absorbed through the tension or compression of the constituent struts. Therefore, the microstructure in nodes position of Octet lattice structures may occur unprecedented evolution process under extreme loading condition compared to the strut position. Moreover, when the feature size goes down to the nanometer scale, due to the experimental difficulties in operating these lattices at small scales, the extreme mechanical behavior and microstructure mechanism of metallic micro/nanolattices are basically unexplored area.

Reconfigurable response: In term of the multifunctional application of the metallic architected materials, extensive research has been devoted to utilizing mechanical metamaterials in diverse areas, such as electrocatalysis, lithium batteries, thermal management, and biomedical engineering. However, it is important to note that the aforementioned applications primarily focus on static operational conditions. The pursuit of programmable response represents an emerging avenue for metallic mechanical metamaterials. When they are integrated with various functional metallic materials, such as shape memory alloy, magnetic materials, and liquid metal, metallic architected exhibits the promising potential to achieve the

adapt and actuate ability thus remarkably broaden their applications space. In addition, the current mechanical and functional are mainly focused on single mechanical metamaterial. The arrayed metallic 3D topological complicated architected materials, when the feature size comparable to the wavelength of optical or acoustic waves, shows enormous potential for the development of acoustic and optical metamaterial.

Scalability and commercial viability: High-precision AM technologies normally can achieve unprecedented levels of control over the scaffold geometry, including unit cell density, wall thickness and the porous size. However, scalable manufacturing with a target topology is a particularly challenging problem, significantly restricting the commercial viability of disordered alloys metamaterial in industrial applications. On the one hand, the advancement of industry 4.0, integrating robotics, automation, and artificial intelligence technologies, can effectively release the full potential of industrial scale AM and shorten product development cycle. The emerging trend is the combination of a subtractive system with AM technology. It can enhance surface finish and minimize defects between the layers, further improving the usability of AM components. In addition to advancing printing speed, self-assembly technology emerges as a promising alternative for achieving scalable manufacturing of nanolattices. It exhibited the potential to explore the unique mechanical, energy conversion and optical properties at large scale lattice structures due to the well-known size effect.

Acknowledgment

This work was financially supported by National Natural Science Foundation of China (Grant No. 52201176), Guangdong Basic and Applied Basic Research Foundation (Grant Nos. 2021A1515111107 and 2022A1515011439), Young Talent Support Project·of Guangzhou Association for Science and Technology (Grant No. QT2024–041), Open Research Fund of Songshan Lake Materials Laboratory (Grant No. 2023SLABFN14), and RGC Collaborative Research Fund of Hong Kong (Grant No. C7074-23G).

Author contributions

X X L and L Q W contributed equally to this work. X X L conceived this work and Y L supervised this work; X X L and L Q W wrote the paper with input and comments from all authors.

Conflict of interest

The authors declare no competing interest.

ORCID iDs

Xinxin Li https://orcid.org/0009-0003-8011-5712
Yang Lu https://orcid.org/0000-0002-9280-2718

References

[1] Ma E and Wu X 2019 Tailoring heterogeneities in high-entropy alloys to promote strength-ductility synergy *Nat. Commun.* **10** 5623
[2] Qiao J C, Wang Q, Pelletier J M, Kato H, Casalini R, Crespo D, Pineda E, Yao Y and Yang Y 2019 Structural heterogeneities and mechanical behavior of amorphous alloys *Prog. Mater. Sci.* **104** 250–329
[3] Parisi G and Sciortino F 2013 Structural glasses: Flying to the bottom *Nat. Mater.* **12** 94–95
[4] Greer A L 2009 Metallic glasses…on the threshold *Mater. Today* **12** 14–22
[5] Telford M 2004 The case for bulk metallic glass *Mater. Today* **7** 36–43
[6] Huang E W and Liaw P K 2019 High-temperature materials for structural applications: new perspectives on high-entropy alloys, bulk metallic glasses, and nanomaterials *MRS Bull.* **44** 847–53
[7] Sun Y and Dai S 2021 High-entropy materials for catalysis: a new frontier *Sci. Adv.* **7** eabg1600
[8] Li M, Lin F, Zhang S, Zhao R, Tao L, Li L, Li J, Zeng L, Luo M and Guo S 2024 High-entropy alloy electrocatalysts go to (sub-)nanoscale *Sci. Adv.* **10** eadn2877
[9] Hsu W L, Tsai C W, Yeh A C and Yeh J W 2024 Clarifying the four core effects of high-entropy materials *Nat. Rev. Chem.* **8** 471–85
[10] Jiang B, Yu Y, Chen H, Cui J, Liu X, Xie L and He J 2021 Entropy engineering promotes thermoelectric performance in p-type chalcogenides *Nat. Commun.* **12** 3234
[11] Ma Y *et al* 2022 Resolving the role of configurational entropy in improving cycling performance of multicomponent hexacyanoferrate cathodes for sodium-ion batteries *Adv. Funct. Mater.* **32** 2202372
[12] Yang B B *et al* 2022 High-entropy enhanced capacitive energy storage *Nat. Mater.* **21** 1074–80
[13] Mozdzierz M, Dabrowa J, Stepien A, Zajusz M, Stygar M, Zajac W, Danielewski M and Swierczek K 2021 Mixed ionic-electronic transport in the high-entropy (Co,Cu,Mg,Ni,Zn)LiO oxides *Acta Mater.* **208** 116735
[14] Ding Q *et al* 2019 Tuning element distribution, structure and properties by composition in high-entropy alloys *Nature* **574** 223–7
[15] Jiang R, Da Y, Chen Z, Cui X, Han X, Ke H, Liu Y, Chen Y, Deng Y and Hu W 2022 Progress and perspective of metallic glasses for energy conversion and storage *Adv. Energy Mater.* **12** 2101092
[16] Wang J-Q, Liu Y-H, Chen M-W, Xie G-Q, Louzguine-Luzgin D V, Inoue A and Perepezko J H 2012 Rapid degradation of Azo Dye by fe-based metallic glass powder *Adv. Funct. Mater.* **22** 2567–70
[17] Wang X *et al* 2020 Glassy Li metal anode for high-performance rechargeable Li batteries *Nat. Mater.* **19** 1339–45
[18] Chang C, Zhang H P, Zhao R, Li F C, Luo P, Li M Z and Bai H Y 2022 Liquid-like atoms in dense-packed solid glasses *Nat. Mater.* **21** 1240–5
[19] Yuan Y *et al* 2022 Three-dimensional atomic packing in amorphous solids with liquid-like structure *Nat. Mater.* **21** 95–102
[20] Hu Y C *et al* 2016 A highly efficient and self-stabilizing metallic-glass catalyst for electrochemical hydrogen generation *Adv. Mater.* **28** 10293–7
[21] Wang Z J, Li M X, Yu J H, Ge X B, Liu Y H and Wang W H 2020 Low-iridium-content IrNiTa metallic glass films as intrinsically active catalysts for hydrogen evolution reaction *Adv. Mater.* **32** e1906384

[22] Jia Z, Kang J, Zhang W C, Wang W M, Yang C, Sun H, Habibi D and Zhang L C 2017 Surface aging behaviour of Fe-based amorphous alloys as catalysts during heterogeneous photo Fenton-like process for water treatment *Appl. Catal.* B **204** 537–47

[23] Greer A L 2011 Metallic glasses: Damage tolerance at a price *Nat. Mater.* **10** 88–89

[24] Inoue A, Shen B, Koshiba H, Kato H and Yavari A R 2003 Cobalt-based bulk glassy alloy with ultrahigh strength and soft magnetic properties *Nat. Mater.* **2** 661–3

[25] Li F C *et al* 2024 Oxidation-induced superelasticity in metallic glass nanotubes *Nat. Mater.* **23** 52–57

[26] Yang Y *et al* 2021 Determining the three-dimensional atomic structure of an amorphous solid *Nature* **592** 60–64

[27] Moniri S *et al* 2023 Three-dimensional atomic structure and local chemical order of medium- and high-entropy nanoalloys *Nature* **624** 564–9

[28] George E P, Raabe D and Ritchie R O 2019 High-entropy alloys *Nat. Rev. Mater.* **4** 515–34

[29] Peters A B, Zhang D, Chen S, Ott C, Oses C, Curtarolo S, McCue I, Pollock T M and Eswarappa Prameela S 2024 Materials design for hypersonics *Nat. Commun.* **15** 3328

[30] Chen K and Li L 2019 Ordered structures with functional units as a paradigm of material design *Adv. Mater.* **31** e1901115

[31] Jiao P, Mueller J, Raney J R, Zheng X R and Alavi A H 2023 Mechanical metamaterials and beyond *Nat. Commun.* **14** 6004

[32] Veselago V G 1968 The electrodynamics of substances with simultaneously negative values of e and μ *Sov. Phys. - Usp.* **10** 509–14

[33] Kadic M, Milton G W, van Hecke M and Wegener M 2019 3D metamaterials *Nat. Rev. Phys.* **1** 198–210

[34] Smith D R, Padilla W J, Vier D C, Nemat-Nasser S C and Schultz S 2000 Composite medium with simultaneously negative permeability and permittivity *Phys. Rev. Lett.* **84** 4184–7

[35] Shelby R A, Smith D R and Schultz S 2001 Experimental verification of a negative index of refraction *Science* **292** 77–79

[36] Schurig D, Mock J J, Justice B J, Cummer S A, Pendry J B, Starr A F and Smith D R 2006 Metamaterial electromagnetic cloak at microwave frequencies *Science* **314** 977–80

[37] Pendry J B, Schurig D and Smith D R 2006 Controlling electromagnetic fields *Science* **312** 1780–2

[38] Sun J B, Shalaev M I and Litchinitser N M 2015 Experimental demonstration of a non-resonant hyperlens in the visible spectral range *Nat. Commun.* **6** 7201

[39] Arbabi E, Arbabi A, Kamali S M, Horie Y, Faraji-Dana M and Faraon A 2018 MEMS-tunable dielectric metasurface lens *Nat. Commun.* **9** 812

[40] Pendry J B *et al* 2000 Negative refraction makes a perfect lens *Phys. Rev. Lett.* **85** 3966–9

[41] Liu Y, Wang Y, Ren H, Meng Z, Chen X, Li Z, Wang L, Chen W, Wang Y and Du J 2024 Ultrastiff metamaterials generated through a multilayer strategy and topology optimization *Nat. Commun.* **15** 2984

[42] Vyatskikh A, Delalande S, Kudo A, Zhang X, Portela C M and Greer J R 2018 Additive manufacturing of 3D nano-architected metals *Nat. Commun.* **9** 593

[43] Sriraman M R, Babu S S and Short M 2010 Bonding characteristics during very high power ultrasonic additive manufacturing of copper *Scr. Mater.* **62** 560–3

[44] Dehoff R R and Babu S S 2010 Characterization of interfacial microstructures in 3003 aluminum alloy blocks fabricated by ultrasonic additive manufacturing *Acta Mater.* **58** 4305–15

[45] Gu D, Shi X, Poprawe R, Bourell D L, Setchi R and Zhu J 2021 Material-structure-performance integrated laser-metal additive manufacturing *Science* **372** eabg1487

[46] Liu S Y and Shin Y C 2019 Additive manufacturing of Ti6Al4V alloy: a review *Mater. Des.* **164** 107552

[47] Kwok C T, Man H C, Cheng F T and Lo K H 2016 Developments in laser-based surface engineering processes: with particular reference to protection against cavitation erosion *Surf. Coat Tech.* **291** 189–204

[48] Perini M, Bosetti P and Balc N 2020 Additive manufacturing for repairing: from damage identification and modeling to DLD *Rapid Prototyp. J.* **26** 929–40

[49] Fujieda T, Shiratori H, Kuwabara K, Kato T, Yamanaka K, Koizumi Y and Chiba A 2015 First demonstration of promising selective electron beam melting method for utilizing high-entropy alloys as engineering materials *Mater. Lett.* **159** 12–15

[50] Kenel C, Casati N P M and Dunand D C 2019 3D ink-extrusion additive manufacturing of CoCrFeNi high-entropy alloy micro-lattices *Nat. Commun.* **10** 904

[51] Chen M, Zhang D, Hsu Y-C and Dunand D C 2024 Microstructure and properties of high-entropy-superalloy microlattices fabricated by direct ink writing *Acta Mater.* **275** 120055

[52] Hu J and Yu M F 2010 Meniscus-confined three-dimensional electrodeposition for direct writing of wire bonds *Science* **329** 313–6

[53] Skylar-Scott M A, Gunasekaran S and Lewis J A 2016 Laser-assisted direct ink writing of planar and 3D metal architectures *Proc. Natl Acad. Sci.* **113** 6137–42

[54] Hirt L, Ihle S, Pan Z J, Dorwling-Carter L, Reiser A, Wheeler J M, Spolenak R, Vörös J and Zambelli T 2016 Template-free 3D microprinting of metals using a force-controlled nanopipette for layer-by-layer electrodeposition *Adv. Mater.* **28** 2311–5

[55] Liu B, Liu S, Devaraj V, Yin Y, Zhang Y, Ai J, Han Y and Feng J 2023 Metal 3D nanoprinting with coupled fields *Nat. Commun.* **14** 4920

[56] Liu S R, Ai J G, Zhang Y Q and Feng J C 2024 Programmable and parallel 3D nanoprinting using configured electric fields *Adv. Funct. Mater.* **34** 2308734

[57] Liu B, Liu Q and Feng J 2024 Operando colorations from real-time growth of 3D-printed nanoarchitectures *Adv. Mater.* **36** 2404977

[58] Kluck S, Hambitzer L, Luitz M, Mader M, Sanjaya M, Balster A, Milich M, Greiner C, Kotz-Helmer F and Rapp B E 2022 Replicative manufacturing of metal moulds for low surface roughness polymer replication *Nat. Commun.* **13** 5048

[59] Jiang Z and Pikul J H 2021 Centimetre-scale crack-free self-assembly for ultra-high tensile strength metallic nanolattices *Nat. Mater.* **20** 1512–8

[60] Cohen A, Bourell D, Chen R, Frodis U, Wu M T and Folk C 2010 Microscale metal additive manufacturing of multi-component medical devices *Rapid Prototyp. J.* **16** 209–15

[61] Chen H L and Grey C P 2008 Molten salt synthesis and high rate performance of the "Desert-Rose" form of LiCoO *Adv. Mater.* **20** 2206–10

[62] Saleh M S, Hu C and Panat R 2017 Three-dimensional microarchitected materials and devices using nanoparticle assembly by pointwise spatial printing *Sci. Adv.* **3** e1601986

[63] Visser C W, Pohl R, Sun C, Roemer G W, In 't Veld B H and Lohse D 2015 Toward 3D printing of pure metals by laser-induced forward transfer *Adv. Mater.* **27** 4087–92

[64] Gorodesky N, Sedghani-Cohen S, Altman M, Fogel O, Cohen-Taguri G, Fleger Y, Kotler Z and Zalevsky Z 2020 Concurrent formation of metallic glass during laser

forward transfer 3D printing *Adv. Funct. Mater.* **30** 2001260
[65] Gorodesky N, Sedghani-Cohen S, Fogel O, Altman M, Cohen-Taguri G, Kotler Z and Zalevsky Z 2022 Printed Cu-Ag phases using laser-induced forward transfer *Adv. Eng. Mater.* **24** 2100952
[66] Hofmann D C, Suh J Y, Wiest A, Duan G, Lind M L, Demetriou M D and Johnson W L 2008 Designing metallic glass matrix composites with high toughness and tensile ductility *Nature* **451** 1085–9
[67] Qiao J, Jia H and Liaw P K 2016 Metallic glass matrix composites *Mater. Sci. Eng.* R **100** 1–69
[68] Wu Y, Xiao Y, Chen G, Liu C T and Lu Z 2010 Bulk metallic glass composites with transformation-mediated work-hardening and ductility *Adv. Mater.* **22** 2770–3
[69] Sarac B and Schroers J 2013 Designing tensile ductility in metallic glasses *Nat. Commun.* **4** 2158
[70] Sopu D, Soyarslan C, Sarac B, Bargmann S, Stoica M and Eckert J 2016 Structure-property relationships in nanoporous metallic glasses *Acta Mater.* **106** 199–207
[71] Ketov S V *et al* 2015 Rejuvenation of metallic glasses by non-affine thermal strain *Nature* **524** 200–3
[72] Pan J, Ivanov Y P, Zhou W H, Li Y and Greer A L 2020 Strain-hardening and suppression of shear-banding in rejuvenated bulk metallic glass *Nature* **578** 559–62
[73] Guo H, Yan P F, Wang Y B, Tan J, Zhang Z F, Sui M L and Ma E 2007 Tensile ductility and necking of metallic glass *Nat. Mater.* **6** 735–9
[74] Kumar G, Desai A and Schroers J 2011 Bulk metallic glass: the smaller the better *Adv. Mater.* **23** 461–76
[75] Jang D C and Greer J R 2010 Transition from a strong-yet-brittle to a stronger-and-ductile state by size reduction of metallic glasses *Nat. Mater.* **9** 215–9
[76] Yang C R, Ouyang D, Zhang L, Zhang Y Y, Tong X, Ke H B, Chan K C and Wang W H 2024 The enhancement of damage tolerance of 3D-printed high strength architected metallic glasses by unit cell shape design *Addit. Manuf.* **85** 104125
[77] Lee S W, Jafary-Zadeh M, Chen D Z, Zhang Y W and Greer J R 2015 Size effect suppresses brittle failure in hollow $Cu_{60}Zr_{40}$ metallic glass nanolattices deformed at cryogenic temperatures *Nano Lett.* **15** 5673–81
[78] Liontas R and Greer J R 2017 3D nano-architected metallic glass: size effect suppresses catastrophic failure *Acta Mater.* **133** 393–407
[79] Liu Z, Chen W, Carstensen J, Ketkaew J, Ojeda Mota R M, Guest J K and Schroers J 2016 3D metallic glass cellular structures *Acta Mater.* **105** 35–43
[80] Zheng X *et al* 2016 Multiscale metallic metamaterials *Nat. Mater.* **15** 1100–6
[81] Wada T, Inoue A and Greer A L 2005 Enhancement of room-temperature plasticity in a bulk metallic glass by finely dispersed porosity *Appl. Phys. Lett.* **86** 251907
[82] Brothers A H and Dunand D C 2005 Plasticity and damage in cellular amorphous metals *Acta Mater.* **53** 4427–40
[83] Brothers A H and Dunand D C 2006 Amorphous metal foams *Scr. Mater.* **54** 513–20
[84] Demetriou M D, Hanan J C, Veazey C, Di Michiel M, Lenoir N, Üstündag E and Johnson W L 2007 Yielding of metallic glass foam by percolation of an elastic buckling instability *Adv. Mater.* **19** 1957–62
[85] Lakes R 1993 Materials with structural hierarchy *Nature* **361** 511–5
[86] Oftadeh R, Haghpanah B, Vella D, Boudaoud A and Vaziri A 2014 Optimal fractal-like hierarchical honeycombs *Phys. Rev. Lett.* **113** 104301
[87] Rayneau-Kirkhope D, Mao Y and Farr R 2013 Optimization of fractal space frames under gentle compressive load *Phys. Rev.* E **87** 063204
[88] Ritchie R O 2011 The conflicts between strength and toughness *Nat. Mater.* **10** 817–22
[89] Hall G S 1984 Chemist's wood *Nature* **310** 521
[90] Ashby M F 2006 The properties of foams and lattices *Phil. Trans. R. Soc.* A **364** 15–30
[91] Rho J Y, Kuhn-Spearing L and Zioupos P 1998 Mechanical properties and the hierarchical structure of bone *Med. Eng. Phys.* **20** 92–102
[92] Bauer J, Schroer A, Schwaiger R, Tesari I, Lange C, Valdevit L and Kraft O 2015 Push-to-pull tensile testing of ultra-strong nanoscale ceramic–polymer composites made by additive manufacturing *Extrem. Mech. Lett.* **3** 105–12
[93] Wang W H 2007 Roles of minor additions in formation and properties of bulk metallic glasses *Prog. Mater. Sci.* **52** 540–96
[94] Li M X, Zhao S F, Lu Z, Hirata A, Wen P, Bai H Y, Chen M, Schroers J, Liu Y and Wang W H 2019 High-temperature bulk metallic glasses developed by combinatorial methods *Nature* **569** 99–103
[95] Yang C, Zhang C, Xing W and Liu L 2018 3D printing of Zr-based bulk metallic glasses with complex geometries and enhanced catalytic properties *Intermetallics* **94** 22–28
[96] Verma P, Shah V, Baldrian P, Gabriel J, Stopka P, Trnka T and Nerud F 2004 Decolorization of synthetic dyes using a copper complex with glucaric acid *Chemosphere* **54** 291–5
[97] Fathima N N, Aravindhan R, Rao J R and Nair B U 2008 Dye house wastewater treatment through advanced oxidation process using Cu-exchanged Y zeolite: a heterogeneous catalytic approach *Chemosphere* **70** 1146–51
[98] Deng J *et al* 2017 Multiscale structural and electronic control of molybdenum disulfide foam for highly efficient hydrogen production *Nat. Commun.* **8** 14430
[99] Sekol R C, Kumar G, Carmo M, Gittleson F, Hardesty-Dyck N, Mukherjee S, Schroers J and Taylor A D 2013 Bulk metallic glass micro fuel cell *Small* **9** 2081–5
[100] Uzun C, Kahler N, de Peralta L G, Kumar G and Bernussi A A 2017 Photo-induced-heat localization on nanostructured metallic glasses *J. Appl. Phys.* **122** 094306
[101] Yu J R, Cheng P, Ma Z Q and Yi B L 2003 Fabrication of miniature silicon wafer fuel cells with improved performance *J. Power Sources* **124** 40–46
[102] Greer A L, Rutherford K L and Hutchings M 2002 Wear resistance of amorphous alloys and related materials *Int. Mater. Rev.* **47** 87–112
[103] Lee S, Kim S W, Ghidelli M, An H S, Jang J, Li Bassi A, Lee S Y and Park J U 2020 Integration of transparent supercapacitors and electrodes using nanostructured metallic glass films for wirelessly rechargeable, skin heat patches *Nano Lett.* **20** 4872–81
[104] Park J, Ahn D B, Kim J, Cha E, Bae B S, Lee S Y and Park J U 2019 Printing of wirelessly rechargeable solid-state supercapacitors for soft, smart contact lenses with continuous operations *Sci. Adv.* **5** eaay0764
[105] Bayata S and Ermertcan A T 2012 Thermotherapy in dermatology *Cutan. Ocul. Toxicol.* **31** 235–40
[106] Dilek B, Gözüm M, Sahin E, Baydar M, Ergör G, El Ö, Bircan Ç and Gülbahar S 2013 Efficacy of paraffin bath therapy in hand osteoarthritis: a single-blinded randomized controlled trial *Arch. Phys. Med. Rehabil.* **94** 642–9
[107] Briers J D 2001 Laser Doppler, speckle and related techniques for blood perfusion mapping and imaging *Physiol. Meas.* **22** R35–R66
[108] Fredriksson I, Larsson M and Strömberg T 2009 Measurement depth and volume in laser Doppler flowmetry *Microvascular Res.* **78** 4–13
[109] Gludovatz B, Hohenwarter A, Catoor D, Chang E H, George E P and Ritchie R O 2014 A fracture-resistant

high-entropy alloy for cryogenic applications *Science* **345** 1153–8
[110] Placone J K and Engler A J 2018 Recent advances in extrusion-based 3D printing for biomedical applications *Adv. Healthcare Mater.* **7** 1701161
[111] Peng S Y *et al* 2021 Additive manufacturing of three-dimensional (3D)-architected CoCrFeNiMn high-entropy alloy with great energy absorption *Scr. Mater.* **190** 46–51
[112] Ren J *et al* 2022 Strong yet ductile nanolamellar high-entropy alloys by additive manufacturing *Nature* **608** 62–68
[113] Feng X B, Surjadi J U, Fan R, Li X C, Zhou W Z, Zhao S J and Lu Y 2021 Microalloyed medium-entropy alloy (MEA) composite nanolattices with ultrahigh toughness and cyclability *Mater. Today* **42** 10–16
[114] Surjadi J U, Feng X, Fan R, Lin W, Li X and Lu Y 2021 Hollow medium-entropy alloy nanolattices with ultrahigh energy absorption and resilience *NPG Asia Mater.* **13** 36
[115] Saccone M A, Gallivan R A, Narita K, Yee D W and Greer J R 2022 Additive manufacturing of micro-architected metals via hydrogel infusion *Nature* **612** 685–90
[116] Ma X R, Duan Y P, Shi Y P, Huang L X and Pang H F 2023 Broadband asymmetric transmission in quasiperiodic-metamaterials based on high entropy alloys ribbon *J. Alloys Compd.* **946** 169349
[117] Shi Y P, Duan Y P, Huang L X, Pang H F, Ma X R, Liu X J and Li Z R 2022 Bio-inspired hierarchical chiral metamaterials: near-field coupling and decoupling effects modulating microwave-stealth properties *Adv. Opt. Mater.* **10** 2200951
[118] Zhao G B, Shao X X, Zhang Q X, Wu Y L, Wang Y N, Chen X, Tian H, Liu Y X, Liu Y P and Lu B H 2023 Porous bio-high entropy alloy scaffolds fabricated by direct ink writing *J. Mater. Sci. Technol.* **157** 21–29
[119] Feng J Y, Wei D X, Zhang P L, Yu Z S, Liu C X, Lu W J, Wang K S, Yan H, Zhang L C and Wang L Q 2023 Preparation of TiNbTaZrMo high-entropy alloy with tunable Young's modulus by selective laser melting *J. Manuf. Process.* **85** 160–5